Available online at www.sciencedirect.com
SCIENCE DIRECT®
Journal of Computational Physics 196 (2004) 145–172
JOURNAL OF COMPUTATIONAL PHYSICS
www.elsevier.com/locate/jcp

Adaptive error control in multi-physical thin-structure MEMS FE-simulation

Jens Müller *, Jan G. Korvink

IMTEK, Institute for Microsystem Technology, Albert Ludwig University, Freiburg, Georges-Koehler-Allee 103, D-79085 Frieburg, Germany

Received 14 March 2002; received in revised form 20 June 2003; accepted 3 November 2003

Abstract

Simulating the physical behavior of thin multi-layered structures accurately is central to micro-electro-mechanical systems (MEMS) CAD. We have produced an automatic method with which to simulate the structural response of multi-layer plate and beam micro-structures accurately and reliably. The method also covers thermo-mechanical and piezoelectric effects. We use a Kirchhoff–Love thin structure model implemented as a conforming Argyris finite element suited for the calculation of thermo-mechanical membrane and bending behavior and which is extended to simulate piezoelectric effects in thin structures. For the first time a posteriori estimation is presented for such multi-layered multi-physically active thin structures. Different sources of errors are identified and specified for several usecases. The error analysis covers locally prestressed regions, plate composition inhomogeneities, geometrical singularities, and singularities conditional upon the presence of source functions of various types. Together with a refinement strategy and a geometrical split pattern the efficiency of the method is demonstrated. Local mesh refinement guarantees the computation of the most accurate solution at a minimum of computational costs.

Keywords: Thin structures; Adaptivity; A posteriori error estimation; Kirchhoff–Love plates; MEMS

1. Introduction

Thin structures are central to micro-electro-mechanical systems (MEMS). Sensors and actuators that constitute MEMS are transducers of signals between different physical energy domains. The transformation therefore involves coupled field effects of which thermo-mechanical and piezoelectric effects are currently among the most important. These effects can be modeled using a thermodynamic approach.

The most frequently used geometries are beam or membrane-like [1]. This requires that the models be reduced to a dimensionality that properly describes the physical behavior of membrane like devices. To accurately simulate such thin structures, we have developed an accurate and stable Kirchhoff–Love (KL)

* Corresponding author. Tel.: +49-761-203-7380; fax: +49-761-203-7382.
E-mail addresses: jmueller@scorec.rpi.edu (J. Müller), korvink@imtek.de (J.G. Korvink).

0021-9991/$ - see front matter © 2003 Elsevier Inc. All rights reserved.
doi:10.1016/j.jcp.2003.11.001

multi-layer plate model implemented as an Argyris finite element [2]. Primarily targeted for MEMS designers, the model enables functional optimization at an early stage of device development, saving resources. The model also encompasses effects that are crucial to the functionality of MEMS.

By extending the primarily mechanical Kirchhoff–Love plate model, first to thermal effects and then to piezoelectric effects, we are able to simulate a wide range of typical MEMS behavior. Hierarchically, the model allows us to simulate thin structure behavior starting from structural mechanics to effects comprising more complex coupling effects. The basic plate model considers the bending field of thin structures only. But since multi-functional thin structures generally consist of several layers the coupling of the membrane field to the bending field also has to be taken into account. This is done by extending the bending equations by the in-plane or membrane field terms. Only in the rare case that the material stacks are perfectly symmetric to the plate's midplane do the in-plane and the out-of-plane displacement fields act independently.

When adding thermal effects by means of a temperature field, there is the option to only consider the bending field or one can choose to couple the temperature field to both the horizontal and the vertical displacement fields. Of course, the choice depends on the specification of boundary conditions. Additionally, the presence of multiple layers within the structure requires the horizontal field to be considered. In our model we only allow for thermal effects in the horizontal direction, neglecting transverse thermal effects. The temperature field therefore can be interpolated on the same elements as the mechanical field. We would like to point out that interlaminar stresses generated by the coefficients of thermal expansion mismatch are not considered in this model. Such stresses are the cause of fracture failure in many MEMS components and in order to cover these correctly a full 3D simulation would become necessary.

Three-dimensional effects are critical for piezoelectric devices, too. The driving and sensing mechanisms of piezoelectrically actuated thin structures are given according to the direct and indirect piezoelectric effect. In the first case the application of a mechanical stress or deformation in absence of an electrical field generates an electrical moment. Conversely, the presence of an electrical field causes the crystal to deform. For thin structures this evidently means that the 2D plate geometry has to be extended in the vertical direction if not only the membrane field shall be considered. Allowing a non-zero component of the electrical field in vertical direction then permits interaction of the bending field and the electrical field either in the direct or indirect way without changing the dimensionality of the displacement fields. This is done by combining the 2D mechanical triangles with 3D electrical prisms. We hereby particularly provide for the case where a piezoelectric layer within the thin structure is driven by different voltages applied on the bottom and on the structure's top layer. Obviously, piezoelectrically active devices require that both the membrane field and the bending field are taken into account since these thin structures generally are multi-layered. Limitations to this model are discussed in detail in Section 3.

The well-known drawback when using the highly sophisticated conforming approach to the Kirchhoff–Love model is the increase of computational cost. All the more this is the case when considering the different coupling effects. In order to reduce these computational expenses we have applied mesh adaptive techniques. By using this method, not only can computational resources be saved, but also the numerical accuracy can be improved. Building upon the pioneer works [3–6] many adaptive finite element techniques for various systems of PDEs have been reported, among them [7] for elliptic systems and [8] for parabolic systems. A recent summary of existing error estimation techniques can be found in the book of Ainsworth and Oden [9].

A posteriori error estimation and mesh refinement techniques proved to be efficient numerical tools for applications in mechanics [10] or solidification processes [11]. For the thin plate problems one usually refers to the classical Zienkiewicz paper [12], such as, e.g. [13]. These papers focus on the treatment of the Reissner–Mindlin type plate, a model presumed to be much more easier for use in engineering practice, an assumption that still is widely discussed. Different viewpoints on which plate model should be favored can be found in [14–22].

For the Kirchhoff–Love model, to our knowledge, adaptive finite element procedures have only been discussed in [7]. In the latter monograph, a posteriori error estimation, the core business when doing adaptive finite elements, is given for a very much simplified plate model equation, namely the bi-Laplacian equation without considering material properties. Neither does this equation represent different material behavior sufficiently when transformed into the weak or variational form, since hereby the plate is assumed to consist of a mono-layered single and homogenous isotropic material, nor does it allow for the treatment of multi-layer structures. These are too restrictive assumptions to be used in general purpose software suitable for MEMS simulation.

We therefore have derived error estimators at first comprising different materials present within a plate structure [23]. We have then extended the methods to multi-layered multi-material thin structures, hereby taking into account the coupling behavior of the horizontal and the vertical field for multi-layers, such as, e.g., the most representative, the bimorph. Then the method has been extended to thermo-mechanical and piezoelectric coupling that give rise to another set of sources of error. In this paper we are going to present the techniques of how to derive these errors. Together with adaptive mesh refinement techniques we are going to demonstrate how to efficiently reduce computational costs and at the same time control the error of the numerical solutions. The purpose of controlling the numerical accuracy is to find, for a given choice of finite element (FE) model, i.e., a geometry and a load case, an adapted mesh whose size and computational error is simultaneously reduced to a minimum. Adaptive meshing requires:

- *A method to quantify the error:* We obtain local error estimates by applying residual techniques [7]. We start from the weak form of the plate equations and derive an error estimator in an energy norm of the mechanical problem. We consider error contributions due to the incompatibility between element internal loads (stresses) and the applied loads. Furthermore, we consider contributions due to shear force, twisting couple and bending moment jumps along inter-element edges for the out-of-plane displacement field. For the in-plane displacement we consider contributions from stress couple jumps along element edges. When taking into account the coupling of the mechanical field to either the temperature field or the electric field by means of piezoelectric effects, additional error sources have to be considered. By combining these contributions consistently, we obtain a reliable and effective element error estimator.
- *A mesh refinement strategy:* We use a ''maximum'' mesh refinement strategy [7]. Those elements are marked to be refined where the weighted element error estimator exceeds the maximum of all individual element error estimator terms.
- *A mesh splitting method:* The refinement process is performed in a way that is governed by the need to preserve shape regularity and to avoid ''hanging nodes''. We use a recursive algorithm, for meshes of triangular finite elements, which is based on the longest edge bisection [24]. Only a finite number of different angles occur during the refinement process and therefore long, thin triangles are avoided.

The paper is organized around these three requirements. Starting with a thermodynamic approach, we develop in Section 2 a variational form of the Kirchhoff–Love plate theory, which we discretize in Section 3 using the Argyris plate element and an appropriate extension for the piezoelectric plate problem. In Section 4 we describe the mesh adaptivity algorithm. In Section 5 we develop the theory for a posteriori error estimation based on the finite element residual, and apply this to the plate discretization. The result is a complete set of element-based (local) contributions that together form the error estimator for the plate element comprising thermal and piezoelectric coupling. In Section 6 we discuss the refinement strategy that we have used, together with the element splitting method to perform mesh modifications locally. We demonstrate the technique, first, by giving a validation of the methods in 7 and with some applications from microsystem technology in Section 8, and summarize our results in the last section. Appendix A recapitulates the most frequently used mathematical and notational conventions that we have used throughout this paper and Appendix B summarizes how the material properties have to be reduced to appropriately describe our thin structure model.

2. Modeling multi-layered thin structures

Many mechanical microsystem components are plate-like or beam-like. They are obtained from semiconductor integrated-circuit manufacturing processes as multi-layer sandwiches. The components' functionalities consist of converting effects from different energy domains. These include effects from the thermal, electrical and the mechanical domains. In this section we outline the main steps in deriving the model.

2.1. Electro-thermo-mechanics

When considering thermodynamically irreversible changes of states we may introduce a set of properties of solids. That is to say, we discuss properties that may be measured with the crystal in equilibrium with its surroundings, so that neither the state of the crystal nor that of its surroundings changes with time. The quantities we shall be concerned with are the temperature T, the electrical field $\boldsymbol{E}$ and the mechanical stress $\boldsymbol{\sigma}$. The electrical field can be expressed as the gradient of some electrostatic potential, $\boldsymbol{E} = -\nabla\phi$. The free energy density $\hat{F}$ then depends on the temperature, the strain and the electrical field

$$\hat{F} = \hat{F}(T, \boldsymbol{\sigma}, \boldsymbol{E}). \tag{1}$$

The differential form for $\hat{F}$ then reads

$$\mathrm{d}\hat{F} = -\hat{S}\,\mathrm{d}T - \boldsymbol{D}\cdot\mathrm{d}\boldsymbol{E} + \boldsymbol{\sigma}\cdot\mathrm{d}\boldsymbol{\epsilon}, \tag{2}$$

where $\hat{S}$ is the entropy density and $\boldsymbol{D}$ is the electrical displacement. The total linear differential of the independent variables $(\boldsymbol{\epsilon}, \boldsymbol{E}, T)$, the strain, the electrical field and the temperature, can be expressed as [25]

$$\begin{aligned}
\mathrm{d}\sigma_{ij} &= \overbrace{\left(\frac{\partial\sigma_{ij}}{\partial\epsilon_{kl}}\right)_{\boldsymbol{E},T}}^{\text{elasticity}}\mathrm{d}\epsilon_{kl} + \overbrace{\left(\frac{\partial\sigma_{ij}}{\partial E_k}\right)_{\boldsymbol{\epsilon},T}}^{\text{inverse piezoelectricity}}\mathrm{d}E_k + \overbrace{\left(\frac{\partial\sigma_{ij}}{\partial T}\right)_{\boldsymbol{\epsilon},\boldsymbol{E}}}^{\text{thermal expansion}}\mathrm{d}T,\\
\mathrm{d}D_i &= \overbrace{\left(\frac{\partial\sigma_{ij}}{\partial\epsilon_{kl}}\right)_{\boldsymbol{E},T}}^{\text{direct piezoelectricity}}\mathrm{d}\epsilon_{kl} + \overbrace{\left(\frac{\partial D_i}{\partial E_j}\right)_{\boldsymbol{\epsilon},T}}^{\text{permittivity}}\mathrm{d}E_j + \overbrace{\left(\frac{\partial D_i}{\partial T}\right)_{\boldsymbol{\epsilon},\boldsymbol{E}}}^{\text{pyroelctricity}}\mathrm{d}T,\\
d\hat{S} &= \overbrace{\left(\frac{\partial\hat{S}}{\partial\epsilon_{ij}}\right)_{\boldsymbol{E},T}}^{\text{piezocaloric effect}}\mathrm{d}\epsilon_{ij} + \overbrace{\left(\frac{\partial\hat{S}}{\partial E_i}\right)_{\boldsymbol{\epsilon},T}}^{\text{electrocaloric effect}}\mathrm{d}E_i + \overbrace{\left(\frac{\partial\hat{S}}{\partial T}\right)_{\boldsymbol{\epsilon},\boldsymbol{E}}}^{\text{heat capacity}}\mathrm{d}T.
\end{aligned} \tag{3}$$

This is a total of 13 equations, each index ranging from 1 to 3. Each of the differential coefficients represents the dependence of the thermodynamic state variables and therefore describes a physical effect. Including higher order derivatives than the linear ones would give rise to additional effects, such as electro-optical effects (non-linear optics), piezo-optical effects such as electrostriction or even elastic moduli of higher order. The coefficients on the leading diagonal of the equations measure the principal effects while the others measure the coupled effects. When deriving symmetries of the coefficients representing the various effects we refer to Eq. (2) which can be rewritten as

$$\mathrm{d}\hat{F} = \left(\frac{\partial\hat{F}}{\partial T}\right)_{\boldsymbol{\epsilon},\boldsymbol{E}}\mathrm{d}T + \left(\frac{\partial\hat{F}}{\partial E_i}\right)_{\boldsymbol{\epsilon},T}\mathrm{d}E_i + \left(\frac{\partial\hat{F}}{\partial\epsilon_{ij}}\right)_{\boldsymbol{\epsilon},T}\mathrm{d}\epsilon_{ij}. \tag{4}$$

Exploiting the second derivatives of the free energy density provides the Maxwell relations which represent the coupling of the different fields. We use $(\pi_{ijk}) = \boldsymbol{\pi}$ for the piezoelectric tensor, $(C_{ijkl}) = \boldsymbol{C}$ for the elasticity

tensor, $(\alpha_{ij}) = \boldsymbol{\alpha}$ for the thermal expansion tensor, $(p_i) = \boldsymbol{p}$ for the pyroelectric tensor, $(\chi_{ij}) = \boldsymbol{\chi}$ for the dielectric permittivity and C_ϵ for the heat capacity at constant strain. The constitutive relations now can be displayed as the integrated form of (3)

$$\begin{aligned}
\sigma_{ij} &= C_{ijkl}\epsilon_{ij} - \pi_{kij}E_k + \alpha_{ij}\Delta T,\\
D_i &= \pi_{ijk}\epsilon_{jk} - \chi_{ij}E_j + p_i\Delta T,\\
\hat{S} &= -\alpha_{ij}\epsilon_{ij} - p_iE_i + (C_\epsilon/T)\Delta T,
\end{aligned} \tag{5}$$

where we have taken into account that changes of states and thus of the variables representing them are dependent on the temperature only in case a temperature change occurs. When introducing the differential balance equations, the following coupled partial differential equations can be obtained:

$$\begin{aligned}
&\nabla\cdot(\boldsymbol{C}:\boldsymbol{\epsilon} - \boldsymbol{\pi}^T:\boldsymbol{E} + \boldsymbol{\alpha}\Delta T) = \boldsymbol{f}_{3D},\\
&\nabla\cdot(\boldsymbol{\pi}:\boldsymbol{\epsilon} - \boldsymbol{\chi}^T\cdot\boldsymbol{E} + \boldsymbol{p}\Delta T) = \rho,\\
&\nabla\cdot(-\boldsymbol{\kappa}\cdot\nabla T) = f.
\end{aligned} \tag{6}$$

The first equation is the conservation of the momentum and $\boldsymbol{f}_{3D}$ is a 3D body force. The second equation is known as the electrostatic Gauss law where ρ is some spatially distributed charge density. The last equation is derived by using Fourier's law of heat conduction which is assumed to be stationary. The symbol f denotes some spatially distributed heat source. The linear strain can be expressed in terms of the mechanical displacement, $\boldsymbol{u} = \boldsymbol{u}_{3D}$,

$$\epsilon_{ij} = \frac{1}{2}\left(\frac{\partial u_i}{\partial x_j} + \frac{\partial u_j}{\partial x_i}\right) = (\nabla\boldsymbol{u})^S_{ij}, \tag{7}$$

S denoting the symmetrization operator, see Appendix A.

2.2. Multi-layered Kirchhoff–Love plates

As a starting point for the derivation of a plate model, we take the weak formulation of 3D mechanics, electrostatics and heat transfer. Multiplication of each of the PDEs (6) with an admissible test function, i.e. a test function that is zero on the essential part of the boundary, and integrating them partially yields

$$\begin{aligned}
&(\boldsymbol{\sigma}_{3D}, \delta\boldsymbol{\epsilon}_{3D}) = (\boldsymbol{f}_{3D}, \delta\boldsymbol{u}_{3D}) + (\boldsymbol{f}_S, \delta\boldsymbol{u}_{3D})_{\partial\Omega_{mech}},\\
&(\boldsymbol{D}, \nabla\psi) = (\rho, \psi) + (h, \psi)_{\partial\Omega_{el}},\\
&(\boldsymbol{\kappa}\cdot\nabla T, \nabla S) = (f, S) + (j, S)_{\partial\Omega_{therm}}.
\end{aligned} \tag{8}$$

The test functions or variational functions from top to bottom are: the 3D variational strain $\delta\boldsymbol{\epsilon}_{3D}$, the variation of the electrostatic potential $\psi = \delta\phi$ and the variation of the temperature field $S = \delta T$. On the right-hand side (RHS), we include the effects of the impressed spatial sources and the boundary conditions for the different energy domains. These consist of a prescribed surface traction $\boldsymbol{f}_S$ on a part of the boundary, prescribed dielectric displacement h and some boundary heat flux j. Our plate models are obtained as the asymptotic case for one of the dimensions of the solid vanishing. We are describing the 3D geometry of the plate as in Fig. 1, or

$$\Omega = \Omega_{3D} = \omega\times[-h/2, h/2] = \{(\boldsymbol{x}, z)/\boldsymbol{x}\in\omega, -h/2\leqslant z\leqslant h/2\}. \tag{9}$$

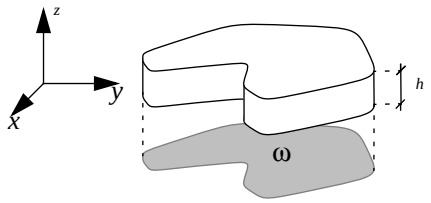

Fig. 1. The 3D geometry of a plate.

The L^2-product for an arbitrary pair of fields u,v on the solid plate is decomposed as

$$(u,v)_{3D} = \int_{-h/2}^{h/2} (u,v)_{\omega}\,\mathrm{d}z. \tag{10}$$

Henceforth, the subscript for the inner product and the integration extrema shall be omitted where there is no ambiguity. The boundary of the solid plate is decomposed as

$$\partial\Omega = \partial\Omega_{3D} = \omega \times \{-h/2\} \cup \omega \times \{h/2\} \cup \partial\omega \times [-h/2, h/2], \tag{11}$$

i.e., into its lower and upper planes and its perimeter wall. For any tensor field $\boldsymbol{A}(\boldsymbol{x}, z)$ defined on the solid plate, we define its nth order moment by

$$\boldsymbol{A}_n(\boldsymbol{x}) = \int z^n \boldsymbol{A}(\boldsymbol{x}, z)\,\mathrm{d}z. \tag{12}$$

In the Kirchhoff–Love theory [26–28], the transverse displacement w is kept constant across the thickness and the in-plane displacement is taken with a linear dependency on z. Additionally, it is necessary to satisfy the constraint that the coefficient of z be the opposite of the gradient of w, expressing the geometrical statement that lines normal to the middle plane keep their orthogonality in the deformed state. The ansatz for the 3D displacement is

$$\boldsymbol{u}_{3\mathrm{D}} = \begin{pmatrix} \boldsymbol{u}(\boldsymbol{x}) - z\nabla w(\boldsymbol{x}) \\ w(\boldsymbol{x}) \end{pmatrix}, \tag{13}$$

where $\boldsymbol{x} = (x, y)$ are the 2D-coordinates.

We now impose the additional condition that the elastic reaction vanishes in the transverse direction of the plate. This implies that only the in-plane components of the stress can be different from zero, so that we may write that

$$\boldsymbol{u}_{3\mathrm{D}} = \begin{pmatrix} \boldsymbol{\sigma} & 0 \\ 0 & 0 \end{pmatrix}. \tag{14}$$

The reduced 2D constitutive relation then reads

$$\boldsymbol{\sigma} = \hat{\boldsymbol{A}} : \boldsymbol{\epsilon} - \hat{\boldsymbol{\pi}}^T : \boldsymbol{E} + \hat{\boldsymbol{\alpha}}\Delta T, \tag{15}$$

where $\hat{\boldsymbol{A}}, \hat{\boldsymbol{\pi}}, \hat{\boldsymbol{\alpha}}$ are the reduced elastic, piezoelectric and thermal conductivity tensors, see Appendix B. The 2D strain can be expressed in terms of the in-plane displacement field and the out-of-plane displacement field

$$\boldsymbol{\epsilon} = (\nabla \boldsymbol{u})^S - z\nabla\nabla w, \tag{16}$$

the latter is also called the plate's bending field. Its variation will be denoted as

$$\delta\boldsymbol{\epsilon} = (\nabla \boldsymbol{v})^S - z\nabla\nabla v. \tag{17}$$

When inserting these relations into the first of Eqs. (8), integration across the thickness of the structures yields the moments (12) of the material tensors and the remaining integrations takes place within the 2D midplane of the structure:

$$\begin{aligned}(\boldsymbol{\sigma}_{3D}, \delta\boldsymbol{\epsilon}_{3D}) &= (\hat{\boldsymbol{A}}_0 : (\nabla \boldsymbol{u})^S - \hat{\boldsymbol{A}}_1 : \nabla\nabla w + (\hat{\boldsymbol{\pi}}^T \cdot \nabla\phi)_0 + (\hat{\boldsymbol{\alpha}}\Delta T)_0, (\nabla \boldsymbol{v})^S) \\ &\quad - (\hat{\boldsymbol{A}}_1 : (\nabla \boldsymbol{u})^S - \hat{\boldsymbol{A}}_2 : \nabla\nabla w + (\hat{\boldsymbol{\pi}}^T \cdot \nabla\phi)_1 + (\hat{\boldsymbol{\alpha}}\Delta T)_1, \nabla\nabla v) \\ &= (\boldsymbol{f}_0, \boldsymbol{v}) - (\boldsymbol{f}_1, \nabla v) + (g_0, v) + (\boldsymbol{M}, \nabla v)_{\partial\omega_{\text{bend}}} + (F, v)_{\partial\omega_{\text{shear}}}.\end{aligned} \tag{18}$$

The body force $\boldsymbol{f}_{3D}$ has been decomposed into the horizontal field $\boldsymbol{f}$ and the vertical field g. The symbols $\boldsymbol{M}$, F denote the bending moments and the shear forces that may be specified on a part of the boundary. The second equation of the system (8) can be rewritten when inserting the relation (16) such that

$$(\hat{\boldsymbol{\pi}} : (\nabla \boldsymbol{u})^S - z\hat{\boldsymbol{\pi}} : \nabla\nabla w - \hat{\boldsymbol{\chi}} \cdot \nabla\phi, \nabla\psi)_\Omega = (\rho, \psi)_\Omega + (h, \psi)_{\partial\Omega_{\text{el}}} \tag{19}$$

holds, having neglected pyroelectric effects. The last equation of the system (8) for the reduced plate model reads

$$(\hat{\boldsymbol{\kappa}}_0 \cdot \nabla T, \nabla S)_\omega = (f_0, S)_\omega + (j_0, S)_\omega. \tag{20}$$

Eqs. (18) and (19) form the electro-mechanical part of coupled thermo-piezoelectric system for multi-layered thin plates. Approximation of the solution of the system by means of an appropriate finite element method has to be done simultaneously for the electrical potential ϕ and the displacement field $(\boldsymbol{u}, w)$. This is not the case for the temperature field T. The entire system can be solved by first computing the temperature field by means of (20) and inserting the result into (18) and (19). We shall point out that the terms

$$\hat{\boldsymbol{\alpha}}\Delta T = \boldsymbol{\sigma}^{\text{ext}} \tag{21}$$

could alternatively be interpreted as some external prestress which may have been caused by the fabrication process of the thin layer.

3. FE-discretization of the coupled multi-layered plate equations

When discretizing the variational problems (18)–(20) one has to bear in mind that in contrast to Eqs. (18) and (20), Eq. (19) has to be discretized on the full 3D domain Ω. Hereby the model allows that different electrostatic boundary conditions be specified on the top and the bottom of the layer-stack. This would not be possible if we also had reduced this equation to the 2D case. Inspecting Eq. (18) shows that, because of the term $(\hat{\boldsymbol{A}}_2 : \nabla\nabla w, \nabla\nabla v)$, the transverse displacement requires that second derivatives also must be square integrable, i.e. $w \in H^2(\omega)$, where $H^2(\omega)$ is the Sobolev space of order two, see Appendix A. In order to have a conforming discretization, the shape functions must also be elements of $H^2(\omega)$, requiring that the shape functions have to be of class $C^1(\omega)$. This can be achieved by implementing the Argyris element [29,30], see Fig. 2.

A vast literature has flourished suggesting several methods to overcome difficulties that are present when using these elements. One of the possible ways would be to utilize the Reissner–Mindlin (RM) (thick-) plate model which only requires $C^0(\omega)-$ elements and therefore is easier to implement. Several sources suggest that the RM model in a number of cases more adequately reflects the physical behavior [31] of thin structures and also when it comes to the reproduction of boundary layers [32,33]. Another way would be to

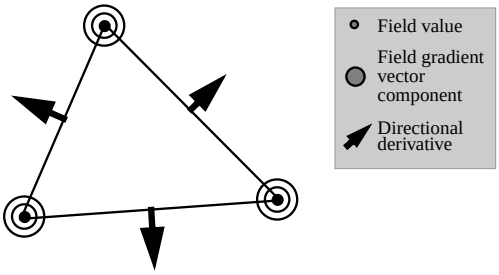

Fig. 2. The Argyris element.

employ one of the non-conforming approaches that have been proposed for the KL model which require that additional steps, undesirable for the use in general purpose software, have to been taken in order to reproduce the solution expected in the thin-plate limit.

Therefore, when using the more sophisticated finite elements of class C^1 a higher degree of reliability of the simulated results can be expected. Additionally, a conforming ansatz for this model has the advantage that error estimators are much simpler to formulate and thus adaptive computations are much faster and more effective in terms of memory requirement. This is in direct contrast to the supposedly efficient non-conforming approaches where the treatment of consistency errors becomes necessary [7,16].

To simultaneously compute the electrical field on a 3D domain and the mechanical and the temperature field on a 2D domain we use a combination of a six-noded prism and an Argyris triangle, see Fig. 3. Since the plate model allows for the treatment of multi-layer stacks we make the arrangement that for a given composite multi-layer the prism's electrical nodes are located in the planes defining both the top and the bottom surface of the structure. The height of all prisms is determined by the largest stack extension present within the multi-layer plate. The nodes for the electrical field for that largest stack then coincide with its vertical margins.

A hypothetical 2D interpolation scheme for the potential would fail either in guaranteeing a continuous solution across the plate or in admitting different potential on the lower and upper faces. On the other hand, limitations to this model clearly are that effects that vary across the thickness other than linearly can not be covered by this approach. This is due to the fact that the values of the electrical field are interpolated only at the upper and lower surface of the structure. Employing this mixed-dimensional approach has the further advantage that linear system condition numbers are kept small as compared to a full 3D approach. Additionally, utilizing a full 3D discretization of the domain, in order to cover both the electric, the mechanical and their coupling effects would require that each layer of the structure be discretized separately, worsening the condition of the linear system even further.

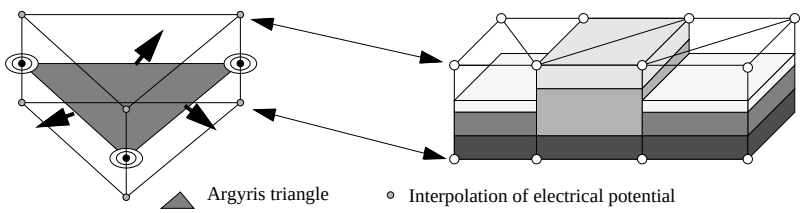

Fig. 3. The combined prism and Argyris triangle finite element. An Argyris triangle is placed exactly on the half way through the thickness of the structure. The electrical field is interpolated between the outmost vertical ends of the structure and thus allows for the specification of boundary conditions that differ at either the top or the bottom of the structure.

4. *h*-adaptive FE-methods

The general idea of adaptive FE-methods is to obtain a numerical solution, within a prescribed tolerance, for a minimum of effort expressed in terms of computer storage and computational time needed by the computing device on hand. As is well known, the solution accuracy of variational boundary value problems (VBVPs) can be improved by either increasing the polynomial degree of the ansatz-space or by increasing the number of elements, i.e., reducing the size of the geometric elements in terms of the mesh-parameter h, which is equal to the element diameter. A major difficulty when using higher order polynomials in the ansatz is that one has to take care of continuity requirements of the secondary fields which are related to the primary fields in terms of their derivatives. More precisely, when interpolating a temperature field on a composite material with Hermitian C^1-elements the thermal fluxes (the gradient of the temperature field contracted with the thermal conductivity tensor) will be discontinuous across material interfaces. The h-adaptive method categorically avoids these difficulties by keeping the initial ansatz-space order but increases the number of elements by locally refining the computational mesh geometrically. The main tools for this purpose are:

- *A posteriori error estimators*, which give global and local information on the error of the numerical solution.
- *Refinement strategies*, used to decide on which regions to refine. The strategies are usually based on an evaluation of local error information.
- *A geometric method*, which specifies how a given region in a mesh is to be refined.

A selective measure would be to refine the discretization near critical regions by adding grid points to areas where the solution is less regular. The question then is: how to identify these regions, and how to keep a good balance between refined and unrefined regions, such that the overall accuracy is optimal. In conjunction with an a posteriori error estimator, an adaptive mesh-refinement process for time independent problems performs the following general steps [7,34]:

1. Construct an initial coarse mesh S_0 of finite elements that represents sufficiently well the geometry of the problem. Put the iteration counter $k = 0$.
2. Solve the discrete problem on S_k.
3. For each finite element T in S_k, compute an a posteriori error estimate.
4. If the estimated global error is sufficiently small, then stop. Otherwise, decide which elements have to be refined and construct the next mesh S_{k+1}. Increment the counter k by one and return to step 2.

5. Error analysis for coupled thin-structure FE-problems

For a given FE-problem, in general, the only data available to the analyst, that can give some indication of the error, is the approximate solution itself. Thus, the challenge is to obtain an a posteriori estimate of the error, i.e., after the initial approximate solution has been obtained. In other words, one has to find an upper bound b_u for the error

$$|||u - u_h||| \leqslant b_u, \tag{22}$$

where $|||\cdot|||$ denotes an energy norm which is defined via the bilinear form a,

$$|||w||| = a(w, w)^{1/2}. \tag{23}$$

The space X in which the weak or variational solution of the problem is sought can be associated with its dual X^* by means of the linear differential operator L of even order $2m$,

$$L : X \to X^*, \quad Lu = f. \tag{24}$$

It turns out that X has to be defined as some Sobolev space or the product space of Sobolev spaces of appropriate order. The bilinear form then can be defined directly by the operator L such that

$$(Lw, v) = a(w, v) \quad \forall w, v \in X \tag{25}$$

holds. The existence of the solution of the VBVP is closely connected to two crucial properties of the bilinear form a, namely that it be continuous and elliptic. These properties will enable us to deal with the different norms in a straightforward manner: the norm in the solution Sobolev space $\|\cdot\|_X$ and the energy norm then are equivalent,

$$\alpha\|v\|_X^2 \leqslant a(v, v) = |||v|||^2 \leqslant K\|v\|_X^2, \tag{26}$$

where K and α are the continuity and the ellipticity constant, respectively. The continuous VBVP then can be formulated in the following way: for a given source function $f \in X^*$ we are looking for the solution u in X such that

$$a(u, v) = (f, v) \quad \forall v \in X. \tag{27}$$

The existence and uniqueness of solutions are then assured by functional analytical results such as the Lax–Milgram theorem, using the continuity and the ellipticity of the bilinear form a. The essential (or Dirichlet) BCs in the following are assumed to vanish identically. This is not a real constraint since any problem with inhomogenous essential BCs can be easily reduced to one with homogenous BCs. Discretizing the problem (27) means choosing a finite-dimensional subspace X_h of X, and looking for an u_h in X_h where

$$a(u_h, v_h) = (f, v_h) \quad \forall v_h \in X_h. \tag{28}$$

This formulation of the FE-problem is the basis of the following abstract a posteriori error analysis. When rewriting (27) with $u - u_h$ instead of u we have for any $v \in X$ by virtue of (25) and the differential equation (24)

$$a(u - u_h, v) = (L(u - u_h), v) = (f - Lu_h, v). \tag{29}$$

For any $w \neq 0$, we can write

$$|||w||| = \frac{1}{|||w|||}|||w|||^2 = \frac{1}{|||w|||}a(w, w) = a\left(w, \frac{w}{|||w|||}\right) \leqslant \sup_{v \in X, |||v|||=1} a(w, v). \tag{30}$$

Combining the last equations (32) and (30) yields the estimate

$$|||u - u_h||| \leqslant \sup_{v \in X, |||v|||=1} a(u - u_h, v) = \sup_{v \in X, |||v|||=1} (f - Lu_h, v). \tag{31}$$

Inequality (31) is an abstract a posteriori error estimator: only known data are required to compute an upper bound for the error $u - u_h$ in the energy norm. The term $f - Lu_h$ defines the residual of the strong form of the partial differential equation. Depending on the shape of the differential operator L we establish computable expressions for the error bound (31). By choosing a Poisson-type equation as in the third of Eqs. (6) to derive an error estimator we gain insight into the mathematical technique without demanding too much formal expenses as it would be the case for the rather complicated coupled plate equations. Later then we are able to treat the plate case just by drawing analogies to the steps which allow of it. We introduce the weak form of a general Poisson problem

$$a(u,v) = \int_\omega \nabla u \cdot \boldsymbol{\kappa} \cdot \nabla v \, \mathrm{d}\boldsymbol{x} = (\tilde{f}, v) \equiv (f, v) + \int_{\Gamma_N} j_N v \, \mathrm{d}\Gamma \quad \forall v \in X, \tag{32}$$

where ω is a bounded domain with polygonal boundary. The part of the boundary where essential boundary conditions are specified is expected to be non-empty whereas normal fluxes j_N across the domain border are specified on the part of the boundary which is denoted as Γ_N. Discretizing the domain by means of an admissible subdivision into triangles we can state the finite element problem as

$$a(u_h, v_h) = \int_\omega f v_h \, \mathrm{d}\boldsymbol{x} + \int_{\Gamma_N} j_N v \, \mathrm{d}\Gamma \quad \forall v_h \in X_h, \tag{33}$$

assuming that given sources coincide with their interpolations, in other words,

$$f = f_h \quad \text{and} \quad j_N = j_{N,h}. \tag{34}$$

The space where the solutions of (31) and (33) have to be sought for in this case are $X = H^1(\omega)$ and a finite-dimensional subspace $X_h \subset H^1(\omega)$ of that Sobolev space. Additionally, we introduce the jump of some function w along an edge E of the triangulation by

$$[w(\boldsymbol{x})] = \lim_{\delta \to 0} \left\{ w(\boldsymbol{x} + \delta \boldsymbol{n}_\Gamma) - w(\boldsymbol{x} - \delta \boldsymbol{n}_\Gamma) \right\}, \tag{35}$$

where $\boldsymbol{n}_\Gamma$ is a fixed outward normal of a given triangle's edge. The scalar product on the RHS of (31) can be recast as ($\tilde{f}$ includes the combined forces of (33))

$$(\tilde{f} - Lu_h, v) = (\tilde{f} - Lu_h, v - v_h) \tag{36}$$

since $X_h \subset X$ and thus the error is orthogonal to X_h, see [29]. Making use of the definition of L in (25) and the definition of a in (32) together with partial integration turns (36) into

$$(\tilde{f} - Lu_h, v - v_h) = (\tilde{f}, v - v_h) - a(u_h, v - v_h) = (\tilde{f}, v - v_h) - \int_\omega \nabla u_h \cdot \boldsymbol{\kappa} \cdot \nabla (v - v_h) \, \mathrm{d}\boldsymbol{x}. \tag{37}$$

The reason for having introduced the term $v - v_h$ instead of v is the fact that we intend to estimate the interpolation error $v - v_h$ in the energy norm which is stronger than the L^2-norm. Partial integration and domain decomposition S, $\bar{\omega} = \bigcup_{T \in S} T$, then yields the expression

$$(\tilde{f} - Lu_h, v - v_h) = (\tilde{f}, v - v_h) - \sum_{T \in S} \left(\int_T \nabla \cdot \boldsymbol{\kappa} \cdot \nabla u_h (v - v_h) \, \mathrm{d}\boldsymbol{x} + \int_{\partial T} \boldsymbol{n} \cdot \boldsymbol{\kappa} \cdot \nabla u_h (v - v_h) \, \mathrm{d}\partial T \right). \tag{38}$$

Using definition (32) and taking into account that integration over edges E in the domain interior occurs twice the above equation becomes

$$\begin{aligned}(\tilde{f} - Lu_h, v - v_h) = \sum_{T \in S} \Bigg(& \int_T (f + \nabla \cdot \boldsymbol{\kappa} \cdot \nabla u_h)(v - v_h) \, \mathrm{d}\boldsymbol{x} + \sum_{E \in \partial T \cap \omega} \frac{1}{2} \int_E [\boldsymbol{n}_E \cdot \boldsymbol{\kappa} \cdot \nabla u_h](v - v_h) \mathrm{d}\Gamma \\ & + \sum_{E \in \partial T \cap \Gamma_N} \int_E j_N - \boldsymbol{n}_E \cdot \boldsymbol{\kappa} \cdot \nabla u_h (v - v_h) \mathrm{d}\Gamma \Bigg).\end{aligned} \tag{39}$$

Applying the Cauchy–Schwarz inequality yields

$$(\tilde{f} - Lu_h, v - v_h) \leqslant \sum_{T\in S} \left(\|f + \nabla\cdot\boldsymbol{\kappa}\cdot\nabla u_h\|_{L^2(\mathrm{T})}\|v - v_h\|_{L^2(\mathrm{T})} + \sum_{E\in\partial T\cap\omega} \frac{1}{2}\|[\boldsymbol{n}_E\cdot\boldsymbol{\kappa}\cdot\nabla u_h]\|_{L^2(\mathrm{E})}\|v - v_h\|_{L^2(\mathrm{E})} + \sum_{E\in\partial T\cap\Gamma_N} \|j_N - \boldsymbol{n}_E\cdot\boldsymbol{\kappa}\cdot\nabla u_h\|_{L^2(\mathrm{E})}\|v - v_h\|_{L^2(\mathrm{E})} \right). \tag{40}$$

We now have to introduce estimates for the terms

$$\|v - v_h\|_{L^2(\mathrm{T})} \quad \text{and} \quad \|v - v_h\|_{L^2(\mathrm{E})}, \tag{41}$$

where v_h denotes some interpolant. As a first difficulty we have already mentioned that the interpolation error has to be estimated in a stronger norm than in the L^2-norm due to (31) which means that also *derivatives* of the error have to be measured. Moreover, we have to cope with the fact that functions in H^1 are not necessarily continuous so that the usual Lagrange interpolation is not valid: pointwise evaluation does not make sense anymore for a field with possible singularities which may very well occur in Sobolev spaces. We avoid this by introducing a special interpolation operator I_h named after Clément [35]. Setting $v_h = I_h v$ we then have the following interpolation estimates:

$$\|v - v_h\|_{L^2(\mathrm{T})} \leqslant c h_{\mathrm{T}} \|\nabla v\|_{L^2(\omega_T)} \tag{42}$$

and

$$\|v - v_h\|_{L^2(\mathrm{E})} \leqslant c h_{\mathrm{T}}^{1/2} \|\nabla v\|_{L^2(\omega_E)}, \tag{43}$$

where c denotes some constant and ω_T the patch of all triangles whose intersection with T is non-empty as sketched in Fig. 4.

Applying these estimates to (40) and making use of the Cauchy–Schwarz inequality once more yields

$$(\tilde{f} - Lu_h, v)^2 \leqslant c \left(\sum_{T\in S} \left(\|f. + \nabla\cdot\boldsymbol{\kappa}\cdot\nabla u_h\|^2_{L^2(\mathrm{T})} h_{\mathrm{T}}^2 + \sum_{E\in S, E\subset\omega} \frac{1}{4}\|[\boldsymbol{n}_E\cdot\boldsymbol{\kappa}\cdot\nabla u_h]\|^2_{L^2(\mathrm{E})} h_{\mathrm{E}} + \sum_{E\in S, E\subset\Gamma_N} \|j_N - \boldsymbol{n}_E\cdot\boldsymbol{\kappa}\cdot\nabla u_h\|^2_{L^2(\mathrm{E})} h_{\mathrm{E}} \right) \right) \|\nabla v\|^2_{L^2(\omega)}, \tag{44}$$

where $h_{\mathrm{T}}, h_{\mathrm{E}}$ denote the triangle diameter and the edge length, respectively. We also have used that

$$\sum_{T\in S} \|\nabla v\|^2_{L^2(\omega_T)} + \sum_{E\subset\left(\omega\cup\Gamma_N\right)} \|\nabla v\|^2_{L^2(\omega_E)} \leqslant c\|\nabla v\|^2_{L^2(\omega)}. \tag{45}$$

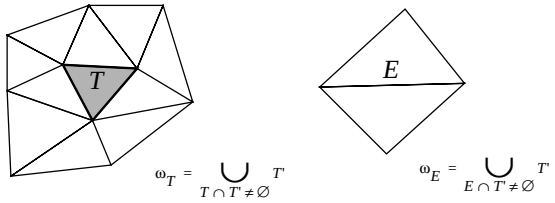

Fig. 4. The domains ω_T and ω_E.

We now consider the fact that the norm in the space X is equivalent to the energy norm of the problem as we assumed in (26). Therefore we can take the supremum of the estimate (44) such that the following local element error estimator:

$$\eta_T^2(u_h) = \|f + \nabla \cdot \boldsymbol{\kappa} \cdot \nabla u_h\|_{L^2(\mathrm{T})}^2 h_{\mathrm{T}}^2 + \sum_{E \in S, E \subset \omega} \frac{1}{4} \|[\boldsymbol{n}_E \cdot \boldsymbol{\kappa} \cdot \nabla u_h]\|_{L^2(\mathrm{E})}^2 h_{\mathrm{E}} + \sum_{E \in S, E \subset \Gamma_N} \|j_N - \boldsymbol{n}_E \cdot \boldsymbol{\kappa} \cdot \nabla u_h\|_{L^2(\mathrm{E})}^2 h_{\mathrm{E}} \tag{46}$$

can be obtained only depending on the computed solution u_h and the given data of the problem. Thus we have shown the a posteriori error estimation

$$|||u - u_h||| \leqslant c \left(\sum_{T \in S} \eta_T^2(u_h) \right)^{1/2} \tag{47}$$

for the energy norm of the error which is reliable and computable. The constant c depends mainly on the smallest angle occurring in the triangulation S [7]. The first term on the RHS of (46) specifies an element residual with respect to the strong form of the problem. In case there is zero load specified, i.e. no heat source is present within the structure only the second addend has to be considered. If in addition linear polynomials are chosen to interpolate the field u, the element residual vanishes completely since second order derivatives of linear functions are identically zero. The second term describes jumps of the gradient across a given edge in the domain interior and might be viewed as a measure of the "smoothness" of the solution whereas the last term considers an error introduced by the deviation of the approximated from the prescribed normal flux along non-essential boundaries. It can be shown that the error estimator (46) not only is reliable in the sense of (47), but also efficient which means that it is bounded from above by the real error [7].

5.1. Error analysis for multi-layered plate problems

Within the above framework we are now able to establish an error estimator for composite plate problems. Therefore we add up the left-hand sides (LHS) of Eqs. (18)–(20) to set up a bilinear form and we add up the corresponding RHS to form the source terms together with the BCs,

$$\begin{aligned} a(\boldsymbol{U}, \boldsymbol{V}) = {} & (\hat{\boldsymbol{A}}_0 : (\nabla \boldsymbol{u})^S - \hat{\boldsymbol{A}}_1 : \nabla\nabla w + (\hat{\boldsymbol{\pi}}^T \cdot \nabla \phi)_0 + (\hat{\boldsymbol{\alpha}} \Delta T)_0, (\nabla \boldsymbol{v})^S) - (\hat{\boldsymbol{A}}_1 : (\nabla \boldsymbol{u})^S \\ & - \hat{\boldsymbol{A}}_2 : \nabla\nabla w + (\hat{\boldsymbol{\pi}}^T \cdot \nabla \phi)_1 + (\hat{\boldsymbol{\alpha}} \Delta T)_1, \nabla\nabla v) + (\hat{\boldsymbol{\pi}} : (\nabla \boldsymbol{u})^S - z\hat{\boldsymbol{\pi}} : \nabla\nabla w - \hat{\boldsymbol{\chi}} \cdot \nabla \phi, \nabla \psi)_\Omega \\ & + (\hat{\boldsymbol{\kappa}}_0 \cdot \nabla T, \nabla S)_\omega = (\boldsymbol{f}_0, \boldsymbol{v}) - (\boldsymbol{f}_1, \nabla v) + (g_0, v) + (\boldsymbol{M}, \nabla v)_{\partial \omega_{\mathrm{bend}}} + (F, v)_{\partial \omega_{\mathrm{shear}}} \\ & + (\rho, \psi)_\Omega + (h, \psi)_{\partial \Omega_{\mathrm{el}}} + (f_0, S)_\omega + (j_0, S)_\omega \\ \equiv {} & (\tilde{\boldsymbol{F}}, \boldsymbol{V}). \end{aligned} \tag{48}$$

Here we have merged the displacement fields, the electrostatic field and the temperature field into a vector valued field $\boldsymbol{U} = (\boldsymbol{u}, w, \phi, T)$ and their variations into $\boldsymbol{V} = (\boldsymbol{v}, v, \psi, S)$. The sources and the Neumann BCs are combined into $\boldsymbol{F}$. Integration over the 3D domain occurs only where explicitly stated by a subscript containing Ω. The appropriate space X in which we have defined the bilinear form is given by

$$X = \{\boldsymbol{U} \in H^1(\omega) \times H^1(\omega) \times H^2(\omega) \times H^1(\omega) \times H^1(\Omega),\ \boldsymbol{U} = 0 \text{ on } \partial\Omega\}. \tag{49}$$

The space X characterizes a mechanically fully clamped thin structure together with overall homogenous essential BCs and thus has to be slightly modified in case we deal with other boundary conditions as follows:

$$X = \{\boldsymbol{U} \in H^1(\omega) \times H^1(\omega) \times H^2(\omega) \times H^1(\omega) \times H^1(\Omega),\ \boldsymbol{U} \text{ satisfies all essential BCs}\}. \tag{50}$$

In fact, only the choice of essential boundary conditions effects the shape of X, whereas Neumann or natural boundary conditions need not to be considered. In order to guarantee the existence of a unique solution we require the essential part of the boundary to be non-empty. Discretization of the VBVP (48) is done according to the requirement that the mechanical and the temperature field are interpolated on a 2D domain whereas the electrical field is interpolated in three dimensions. The domain therefore is subdivided into a layer of prisms, see Fig. 3. The computed solution, consisting of the set of coupled fields is denoted as $\boldsymbol{U}_h$. Applying the estimate (31) to the error of the coupled fields then reads

$$|||\boldsymbol{U}-\boldsymbol{U}_h||| \leqslant \sup_{\boldsymbol{V}\in X,|||\boldsymbol{V}|||=1} a(\boldsymbol{U}-\boldsymbol{U}_h,\boldsymbol{V}) = \sup_{\boldsymbol{V}\in X,|||\boldsymbol{V}|||=1} (\boldsymbol{F}-L\boldsymbol{U}_h,\boldsymbol{V}), \tag{51}$$

where the energy norm here is induced by the bilinear-form a,

$$|||\boldsymbol{U}-\boldsymbol{U}_h|||^2 = a(\boldsymbol{U},\boldsymbol{U}). \tag{52}$$

In order to further simplify the exposition we now make the following definitions which incorporate the computed fields:

$$\begin{aligned}
&\boldsymbol{\sigma}_{\boldsymbol{u}0} = \hat{\boldsymbol{A}}_0 : (\nabla \boldsymbol{u}_h)^S, \quad \boldsymbol{\sigma}_{\boldsymbol{u}1} = \hat{\boldsymbol{A}}_1 : (\nabla \boldsymbol{u}_h)^S, \quad \boldsymbol{\sigma}_{P\phi} = -\hat{\boldsymbol{\pi}}^T \cdot \nabla\phi_h,\\
&\boldsymbol{D}_{Pw} = \hat{\boldsymbol{\pi}}_0 : \nabla\nabla w_h, \quad \boldsymbol{\sigma}_{w1} = \hat{\boldsymbol{A}}_1 : \nabla\nabla w_h, \quad \boldsymbol{\sigma}_{w2} = \hat{\boldsymbol{A}}_2 : \nabla\nabla w_h,\\
&\boldsymbol{D}_{P\boldsymbol{u}} = \hat{\boldsymbol{\pi}} : (\nabla \boldsymbol{u}_h)^S, \quad \boldsymbol{D}_{P\phi} = \hat{\boldsymbol{\chi}} \cdot \nabla\phi_h.
\end{aligned} \tag{53}$$

Carrying out steps (36)–(46) yields an error estimation for the fully coupled multi-physical multi-layered plate structures that, according to (51) satisfies

$$|||\boldsymbol{U}-\boldsymbol{U}_h||| \leqslant c\left(\sum_{T\in S}\eta_T^2(\boldsymbol{U}_h)\right)^{1/2}. \tag{54}$$

The element error estimator $\eta_T(\boldsymbol{U}_h)$ in the same manner as that for the Poisson equation primarily consists of element residuals that measure the difference of some prescribed sources from the computed values. Another contribution are the jumps of quantities such as fluxes or bending moments. These quantities are defined as higher order field derivatives contracted with the corresponding material tensors. The derivative's order is the same as that of those describing the Neumann BCs. Finally there are those contributions which directly measure the deviation of the prescribed Neumann BCs from the computed values. This means that even though vanishing natural BCs do not need to be considered in FE-computations the deviations of these zero values from the calculated values usually are a source of error. This is in contrast to the essential BCs which directly enter the ansatz-space such that these are always fulfilled and do not contribute to the discretization error. The components of the element error estimator $\eta_T(\boldsymbol{U}_h)$ and their description are displayed in Table 1. The L^2-integrations extend over different domains, triangles, triangle edges, prisms, and prism faces abbreviated by T, E, P, F, respectively. Element dimensions h are either triangle diameters and triangle edge lengths $h_{\mathrm{T}}, h_{\mathrm{E}}$ or prism diameters and prism face diameters $h_{\mathrm{P}}, h_{\mathrm{F}}$.

We shall point out that there are other terms that formally have to be considered. These are those involving the horizontal mechanical body force field that we assume to be zero in our computations. Additionally we have neglected terms containing the electrical charge density. Other terms that do not appear in Table 1 are those containing deviations of computed boundary values from the prescribed. Here we have restricted the exposition to the most frequently used conditions in practice. Due to the complexity of the

Table 1
Contributions to the element error estimator

Expression		Field	Description
$\|\nabla\cdot(\nabla\cdot\boldsymbol{\sigma}_{w2})-g_0\|^2_{L^2(\mathrm{T})}h_\mathrm{T}^4$	(55)	w	This element residual for single-layer plates, thickness h, consisting of an isotropic material reads $D\Delta^2 w-g_0$, D denoting the plate's flexural rigidity and Δ^2 the well-known bi-Laplacian operator. It measures the difference between the bi-Laplacian of the out-of plane displacement field from some imposed pressure difference or gravitational force
$\|\nabla\cdot\boldsymbol{\sigma}_{w1}\|^2_{L^2(\mathrm{T})}h_\mathrm{T}^4$	(56)	w	Measures element residual of forces present when computing mechanical deformation of structures at least two layers thick
$\|\nabla\cdot\boldsymbol{\sigma}_{\boldsymbol{u}1}+\boldsymbol{f}_0\|^2_{L^2(\mathrm{T})}h_\mathrm{T}^4$	(57)	$\boldsymbol{u}$	Element residual considering the deviation of computed in-plane body force from the prescribed force $\boldsymbol{f}_0$
$\|[\boldsymbol{n}\cdot\nabla\cdot\boldsymbol{\sigma}_{w2}]\|^2_{L^2(\mathrm{E})}h_E^3$	(58)	w	Jumps of shear forces across element edges which are unphysical
$\|[\boldsymbol{n}\cdot\boldsymbol{\sigma}_{w2}]\|^2_{L^2(\mathrm{E})}h_\mathrm{E}$	(59)	w	Unphysical jumps of bending moments across element edges
$\|[\boldsymbol{n}\cdot\boldsymbol{\sigma}_{\boldsymbol{u}0}]\|^2_{L^2(\mathrm{E})}h_E^3$	(60)	$\boldsymbol{u}$	Inter-element jumps of stress resultants
$\|[\boldsymbol{n}\cdot\boldsymbol{\sigma}_{\boldsymbol{u}1}]\|^2_{L^2(\mathrm{E})}h_\mathrm{E}$	(61)	$\boldsymbol{u}$	Inter-element jumps of in-plane stress resultants, non-zero only for multi-layer structures that are unsymmetrical to the plate's mid-plane
$\|[\boldsymbol{n}\cdot\nabla\cdot\boldsymbol{\sigma}_{\boldsymbol{u}1}]\|^2_{L^2(\mathrm{E})}h_E^3$	(62)	$\boldsymbol{u}$	Jumps of in-plane bending moments
$\|[\boldsymbol{n}\cdot\boldsymbol{\sigma}_{w1}]\|^2_{L^2(\mathrm{E})}h_E^3$	(63)	w	Jumps of bending moments of the flexural field. The second-order derivatives of w are contracted with the first-order moments of the elasticity tensor. This contribution is vanishing for single layered structures
$\|\boldsymbol{n}\cdot\nabla\cdot\boldsymbol{\sigma}_{w2}+F\|^2_{L^2(\mathrm{E})}h_E^3$	(64)	w	Deviations of prescribed shear forces on a part of the boundary from the computed values $\boldsymbol{n}\cdot\nabla\cdot(\hat{\boldsymbol{A}}_2:\nabla\nabla w_h)$
$\|\boldsymbol{M}-\boldsymbol{n}\cdot\boldsymbol{\sigma}_{w2}\|^2_{L^2(\mathrm{E})}h_\mathrm{E}$	(65)	w	Deviations of prescribed bending moments on a part of the boundary from the computed values $\boldsymbol{n}\cdot(\hat{\boldsymbol{A}}_2:\nabla\nabla w_h)$
$\|f+\nabla\cdot\boldsymbol{\kappa}\cdot\nabla T_h\|^2_{L^2(\mathrm{T})}h_\mathrm{T}^2$	(66)	T	Element residual of the heat source. In case the temperature field is interpolated with linear Lagrangian elements and the element heat source is zero this term also will vanish identically
$\|[\boldsymbol{n}\cdot\boldsymbol{\kappa}\cdot\nabla T_h]\|^2_{L^2(\mathrm{T})}h_\mathrm{E}$	(67)	T	Jumps of heat fluxes across element boundaries, physically not allowed
$\|j_N-\boldsymbol{n}\cdot\boldsymbol{\kappa}\cdot\nabla T_h\|^2_{L^2(\mathrm{T})}h_\mathrm{E}$	(68)	T	Deviation of prescribed heat flux j_N across a part of the boundary from the computed flux $\boldsymbol{n}\cdot\boldsymbol{\kappa}\cdot\nabla T_h$
$\|\nabla_{2D}\cdot\boldsymbol{\sigma}_{P\phi}\|^2_{L^2(\mathrm{P})}h_\mathrm{P}^5$	(69)	ϕ	Element residuals measuring errors present in the inverse piezoelectric effect. These contributions are measured on a prism since the electrical field extends over the whole 3D domain. The term (70) vanishes identically since for the electrostatic potential linear interpolation functions are used and second-order derivatives applied on them are identically zero
$\|\nabla_{2D}\cdot(\nabla_{2D}\cdot z\boldsymbol{\sigma}_{P\phi})\|^2_{L^2(\mathrm{P})}h_\mathrm{P}^5$	(70)		
$\|\nabla_{3\mathrm{D}}\cdot\boldsymbol{D}_{P\boldsymbol{u}}\|^2_{L^2(\mathrm{P})}h_\mathrm{P}^2$	(71)		Element residuals in the direct piezoelectric effect. Although both displacement fields are defined on a 2D domain integration takes place over the full 3D domain. See (19) or (49)
$\|\nabla_{3\mathrm{D}}\cdot z\boldsymbol{D}_{Pw}\|^2_{L^2(\mathrm{P})}h_\mathrm{P}^2$	(72)	w	

Table 1 (*continued*)

Expression		Field	Description
$\|\|[\boldsymbol{n}_{2D}\cdot\boldsymbol{\sigma}_{P\phi}]\|\|^2_{L^2(\mathrm{F})}h_{\mathrm{F}}^4$	(73)		Jumps of stresses caused by the inverse piezoelectric effect across element boundaries. These are measured along a prism's rectangular face. Note that the piezoelectric tensor $\hat{\boldsymbol{\pi}}$ may vary through the thickness of the layer as well as the electrostatic potential
$\|\|[\boldsymbol{n}_{2D}\cdot z\boldsymbol{\sigma}_{P\phi}]\|\|^2_{L^2(\mathrm{F})}h_{\mathrm{F}}^2$	(74)	ϕ	
$\|\|[\boldsymbol{n}_{2D}\cdot\nabla_{2D}\cdot z\boldsymbol{\sigma}_{P\phi}]\|\|^2_{L^2(\mathrm{F})}h_{\mathrm{F}}^2$	(75)		
$\|\|[\boldsymbol{n}_{3\mathrm{D}}\cdot\boldsymbol{D}_{P\boldsymbol{u}}]\|\|^2_{L^2(\mathrm{F})}h_{\mathrm{F}}^2$	(76)	$\boldsymbol{u}$	Inter element jumps of the dielectric displacement present in the direct piezoelectric effect caused by the in-plane displacement field
$\|\|[\boldsymbol{n}_{3\mathrm{D}}\cdot z\boldsymbol{D}_{Pw}]\|\|^2_{L^2(\mathrm{F})}h_{\mathrm{F}}$	(77)	w	Inter element jumps of the dielectric displacement present in the direct piezoelectric effect caused by the out-of-plane displacement field
$\|\|[\boldsymbol{n}_{3\mathrm{D}}\cdot z\boldsymbol{D}_{P\phi}]\|\|^2_{L^2(\mathrm{F})}h_{\mathrm{F}}$	(78)	ϕ	Jumps of the dielectric displacement caused by the electrical field itself

thin structure model equations the number of contributing terms is high and reducing the error to the most significant contributions is the subject of current and future investigations.

Alternatively, it might be worthwhile investigating whether different types of error estimators, such as, for example, the gradient recovery based error estimator of Zienkiewicz and Zhu [6] (known for its reliability and efficiency and its easy way to be implemented) perform as well as ours and that possibly at a far lesser cost of implementation. In that case we would like to emphasize that for our equations not only gradients but also second order derivatives would have to be recovered. The presence of the coupling effects and the multi-layered and multi-physical nature of the structure will add further implementation and computational cost to a possible recovery based error estimator. Finally we want to point out that in certain cases its use is known to fail [9] and some caution must be applied.

6. Refinement strategy and split patterns

From heuristic arguments we know that among all partitions of a linear finite element discretization, that one is optimal which equilibrates the error i.e., the errors in all elements should be made equal to or less than the required maximum required error. Among others, the most popular realization is called the maximum strategy and is done in the following manner [24].

Suppose that for a given mesh a solution and an error estimator η_T for each element T have been computed. Put $\eta \equiv \max_{T\in S}\eta_T$ and split an element T if $\eta_T \geqslant \xi\eta$, where ξ is a prescribed threshold, $0 < \xi < 1$. This strategy, applied iteratively, would continue indefinitely. A halting condition is straightforward to add: stop if $\eta \leqslant \eta_{\mathrm{accept}}$.

We have used a value of $\xi = 0.5$ in all of the subsequently presented examples and the number of refinement cycles is determined such that in the very last step of the refinement cycle the predefined error threshold, a fraction of the error obtained in the initial step, is met.

The way in which the refinement process is performed, from a geometrical point of view, depends on the kind of elements present in the mesh. Difficulties arise from keeping shape regularity and from handling hanging nodes. Many rules have been established for the splitting of simplicial mesh constituents, such as, e.g. the ''red'', ''green'' or ''blue'' refinement for triangles. We use a recursive algorithm for triangles which is based on the longest edge bisection, see Fig. 5. It has been shown that only a finite number of different angles occur during the refinement process and therefore shape regularity is guaranteed [36,37]. The algorithm to recursively refine a triangular element is:

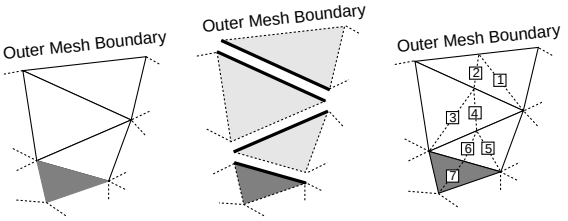

Fig. 5. The elementary mesh at the left consists of four triangles. The shaded triangle is marked to be split along its longest edge. The longest edges of each triangle are marked by thick lines in the center figure. The dashed lines at the right show how the recursive bisection algorithm produces new triangles, continuing through the neighborhood until a first edge can be split (in the worst case, this happens only when the boundary edge is reached), then backtracking. The boxed numbers label the order in which new edges are introduced on the return path of the recursive algorithm.

1.0 do until the neighbor has a compatible refinement-edge:
  1.1 if the neighbor has a non-compatible refinement-edge:
    1.1.1 recursive refine the neighbor.
2.0 bisect both triangles at the refinement-edge. Compatibility is given if the neighbor element's longest edge is at the same time the longest edge of the target element or is a part of the boundary. The terminating recursive algorithm modifies the vicinity of the target element until its edge can be split as sketched in Fig. 5.

Although there are alternatives to this approach, such as the constraint Delaunay method [38] or the advancing front approach [39] our method carries the advantage of allowing the mesh to be represented within the hierarchic computational data structure of binary trees. Unique element data, such as material properties can be fast and easily transferred onto the refined mesh during the computing process.

7. Validation

We demonstrate the performance of our method on selected examples from microsystem technology (MEMS). The following example is more general and serves to demonstrate the efficiency and reliability of the error estimator. For an L-shaped polygon, as depicted in Fig. 6, the solution to the Laplace equation, the third equation of (8), is sought, with Dirichlet BCs $T = 0$ on the bottom at $y = 0$; and on the upper right boundary $T = 1$ at $x = 1$.

The analytical solution that coincides with the weak solution can be obtained via the well known Schwarz–Christoffel transformation [40], that numerically is carried out by the tool matlab [41]. We compare the absolute (i.e. exact) error $T - T_h$ for two different situations during the refinement process. In the first case the approximate solution T_h is obtained by successive *adaptive* refinement according to the algorithms described earlier in this article. In the second case the approximate solution is obtained by a FE-analysis on meshes where all elements are of the same size and in each step the number of elements is *uniformly* increased. On the left side in Fig. 6 the final meshes of both procedures are shown, together with the isothermal lines of the approximated temperature field. The initial mesh is the same in both cases. In the graph on the bottom right the absolute errors are compared for different mesh sizes. For meshes that feature the same number of elements, the absolute error of the approximate fields are considerably higher for the uniform mesh. The estimated error according to Eq. (46) is also shown in the graph. The horizontal arrow in the figure demonstrates the high level of efficiency of the adaptive method in the sense that a more accurate solution can be obtained with a smaller mesh and hence smaller amount of computational effort.

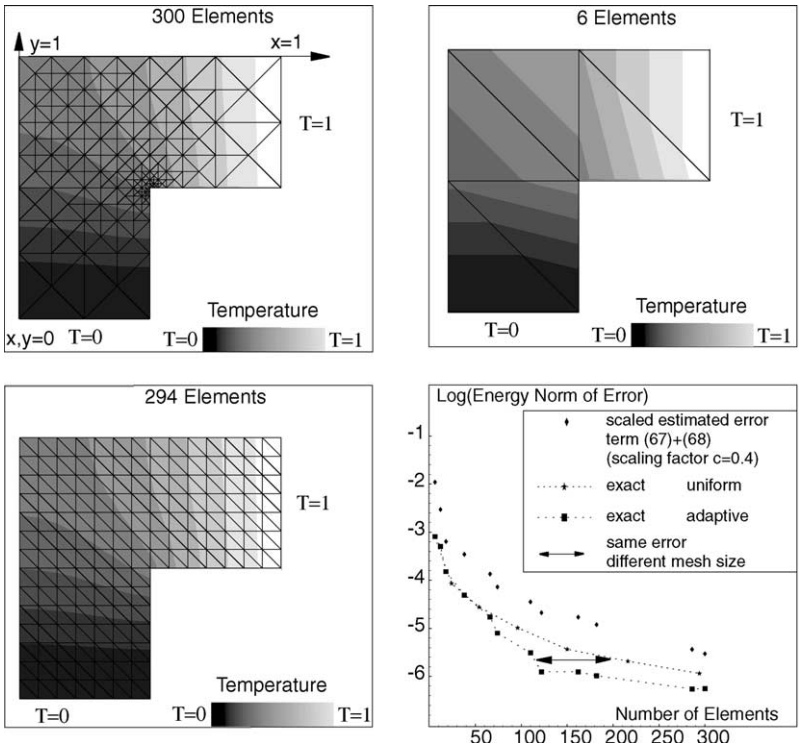

Fig. 6. Uniform and adaptive thermal FE-analysis for an L-shaped domain.

This observation can be further substantiated. When assessing the performance of an error estimator, one very important parameter that can be computed is the *effectivity index* [42,43]. It is the ratio of the estimated error and the true error and can be expressed as

$$\tau = \frac{\sqrt{\sum_{T\in S}\eta_T^2}}{|||u-u_h|||}, \tag{79}$$

η_T denoting the elementwise defined error estimator. Ideally, when the *estimated* error coincides with the exact error, this ratio should be equal to one. In our case, however, and according to inequality (54), we can expect the effectivity index to converge to some constant c. Fig. 7 depicts the value of τ along with the estimated error and the exact exact error during the refinement process. The ratio can, within bounds, be considered to represent some constant value and hence some confidence is given that the error estimator can be trusted when being applied to problems where analytical solutions are not accessible.

Another very important index that reflects the performance and efficiency of the refinement scheme employed is the *rate of convergence* of the error norm of the solution, see for example, [44]. In general, the error norm of the solution is reduced at a given rate p,

$$\|u-u_h\|_m \leqslant ch^p, \quad p = k+1-m > 0, \tag{80}$$

where $2m$ is the PDE order and $\|\cdot\|_m$ accordingly is the H^m-norm of the error. c is a constant and k is the polynomial order of the interpolation functions. This estimate implies that the error goes to zero at the pth power of h as h is decreased. However, such optimal convergence rate will be reduced in the presence of

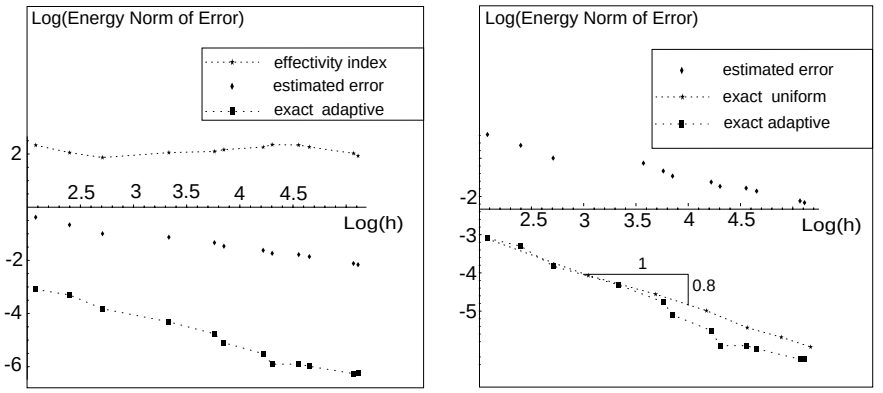

Fig. 7. Effectivity index (left) and convergence rate for the L-shaped domain with linear triangles and the residual error estimator.

singularities such as the re-entrant corner in the example above. An adaptive refinement scheme is said to be effective if it can eliminate the effect of the singularity and restore the optimal convergence rate.

According to (80), the negative logarithm of the error in the energy norm ($m = k = 1$, $p = 1$ in our example, the energy norm then is equivalent to the H^1-norm) versus the negative logarithm of h (in our case expressed in terms of $1/\sqrt{\mathrm{DOF}}$, DOF denoting the number of degrees of freedom) is a straight line whose slope is $-p$. The optimal convergence rate in our case therefore is, expressed in terms of the slope, -1. In Fig. 7 we observe, due to the presence of the singularity, that the slope corresponding to the uniform refinement does not reach the optimal convergence rate. The adaptive refinement scheme, on the other hand, converges at a rate which is close to one and therefore represents strong support for our adaptive refinement scheme.

8. Applications

We have applied these simulation techniques to various multi-physically active thin structures most widely used in MEMS. The simulation requirements range from elementary thermal and pure mechanical analysis to the analysis of thermo-mechanically or piezoelectrically driven devices. Technical aspects of the devices considered can be found in [45,46] and the references therein.

8.1. Thermal structures

As a first application we consider a flat plate consisting of two different material stacks, as sketched in Fig. 8. Typically such structures are used to realize resonant beams as implemented in gas-sensors or atomic force microscope probes [47] or [48]. The gray region consists of polysilicon on a silicon oxide layer while the other part only consists of a silicon oxide layer. The polysilicon part is heated at a rate of $6e13$ (W/m^3), resulting in a temperature distribution according to the BCs specified. We have assumed that the structure is in contact with a heat reservoir at the right end and is thermally isolated on the rest of the boundary. The adaptive simulation procedure starts with an initial coarse mesh also displayed in Fig. 8. The reduction of the estimated error is shown in Fig. 9 by means of the only two contributions to the elements' errors: the jumps of the heat flux across element edges together with boundary inconsistencies of the heat flux (67) and (68) and the element residuals (66). The total estimated error is computed using (47), first summing up the partial contributions to one element error and then summing over the whole mesh. We shall emphasize that

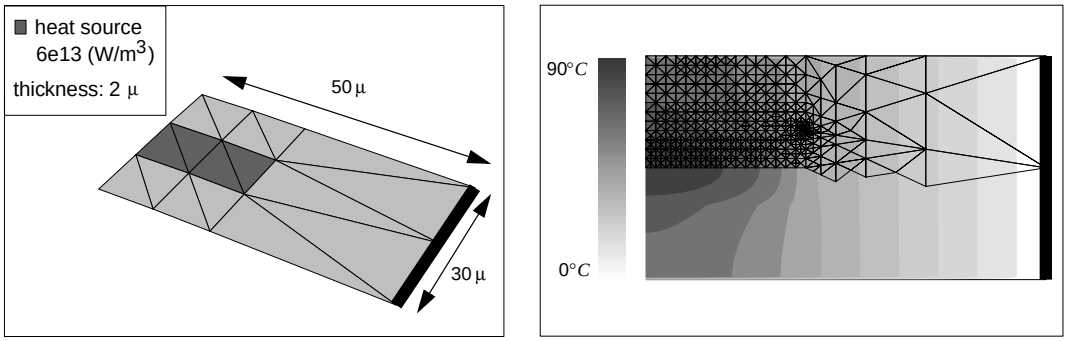

Fig. 8. Mesh and geometry used to compute the initial temperature distribution (left). The right-hand side graphics shows the temperature distribution computed after eleven refinement steps. For clarity half of the underlying mesh has been removed. The major refinement occurs near the corners where different material stacks meet. The thick-lined boundary indicates contact with a heat reservoir whereas the remaining part of the boundary is thermally isolated.

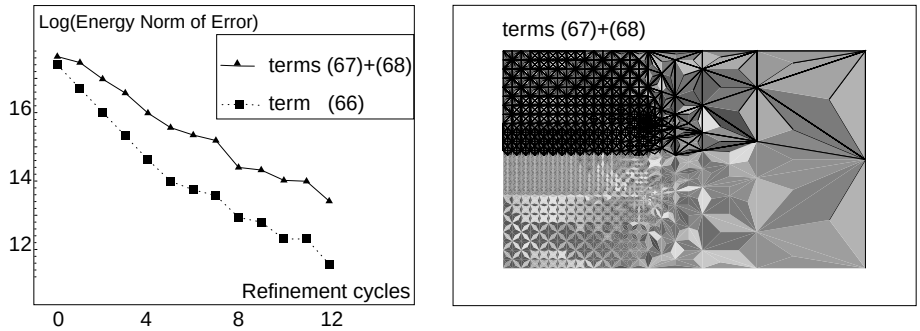

Fig. 9. Logarithmic plot of the only two error contributions present when calculating the temperature distribution in the absence of the other fields. The contribution arising from unphysical jumps of the heat fluxes across element boundaries together with the inaccuracies at the Neumann boundary is higher than the element residuals. The RHS figure depicts the spatial distribution of the jump errors after 12 refinement cycles. The bright areas denote low error values.

the element residual contribution is only present within the heated subdomain since we have interpolated the temperature field by linear elements such that for zero source function the term (66) vanishes. As can be seen in Fig. 8 the major refinement takes place near the corners where different material stacks meet. The nature of these singular points are a combination of the contact of different materials and the wedge-corner singularity, see Section 7, as is well known from early FE-analysis [49].

8.2. Thermo-mechanical structures

In the second example we consider a multi-layered thin structure typical in MEMS used for the detection and the generation of ultrasound such as, for example in [50]. It consists of a silicon oxide and aluminum layer on the outer region, each 0.5 μm thick, and with a lateral dimension of 200 μm as depicted in Fig. 10. The center region is partly covered by a polysilicon layer and serves as a heater. The excitation principle of this device is that energy is dissipated in the polysilicon layer. The heating causes the structure to deform and thanks to the multi-layer arrangement (multimorph) there is, besides the thermal expansion in horizontal direction, a 3D bending of the structure, also presented in Fig. 10. We have simulated the thermo-

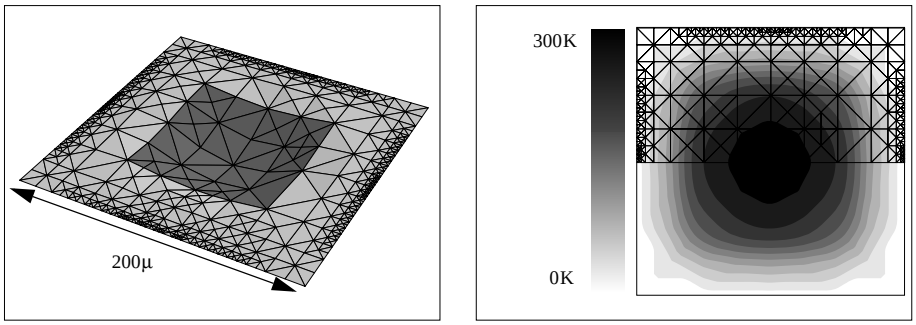

Fig. 10. Exaggerated mechanical deformation computed on a refined grid after 12 refinement cycles. The structure is mechanically clamped on each side. The RHS figure shows a contour plot of the out-of-plane displacement field computed on the same refined mesh.

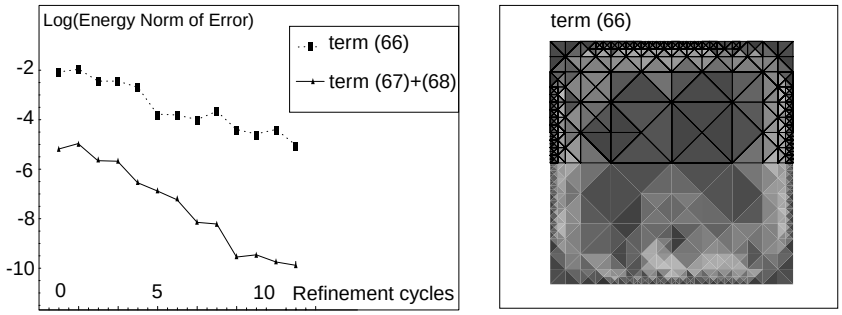

Fig. 11. Errors caused by numerical inaccuracies present in the thermal part of the coupled thermo-mechanical thin plate problem. Dominant in this example are the element residuals describing the deviation of the computed heat force from the one that is prescribed. This contribution is also displayed as a 2D distribution on the right. The brighter the shade is the lower is the error value. The total estimated error approximately coincides with the dominant contribution and therefore is not declared separately.

mechanical behavior starting with a coarse mesh consisting of 16 elements. The numerical solution then is improved in a cycle of 12 steps according to the error reduction plotted in Figs. 11 and 12. The dominant contribution to the total estimated error are the element residuals describing the deviation of the computed heat generation rate from the prescribed. The mechanical errors in this example are much smaller. Nevertheless, other structural configurations may result in a different weighting of each contribution. As far as the mechanical contribution is concerned, the membrane field, in this particular case, exhibits higher errors than the bending field, see Fig. 12.

The membrane field errors are dominated by element residuals considering in-plane body forces that should physically not be present. Smaller are inter-element jumps of stress resultants and in-plane bending moments. The errors caused by the bending field are highest for the inner element shear forces associated with the first order moments of the elasticity tensor, hereby taking into account that the coupling effect of the horizontal and the vertical displacement field is present since the structure is multi-layered. The thermal element residuals that dominate the estimated error are highest near the center of each boundary line, causing the major refinement to be performed in these regions, see Fig. 11.

8.3. Piezoelectric structures

The third application uses a piezoelectric driving mechanism. Transducers of that kind are reported of in [51]. Among others, the working principle might be that of a pressure sensor or that of a pump when used

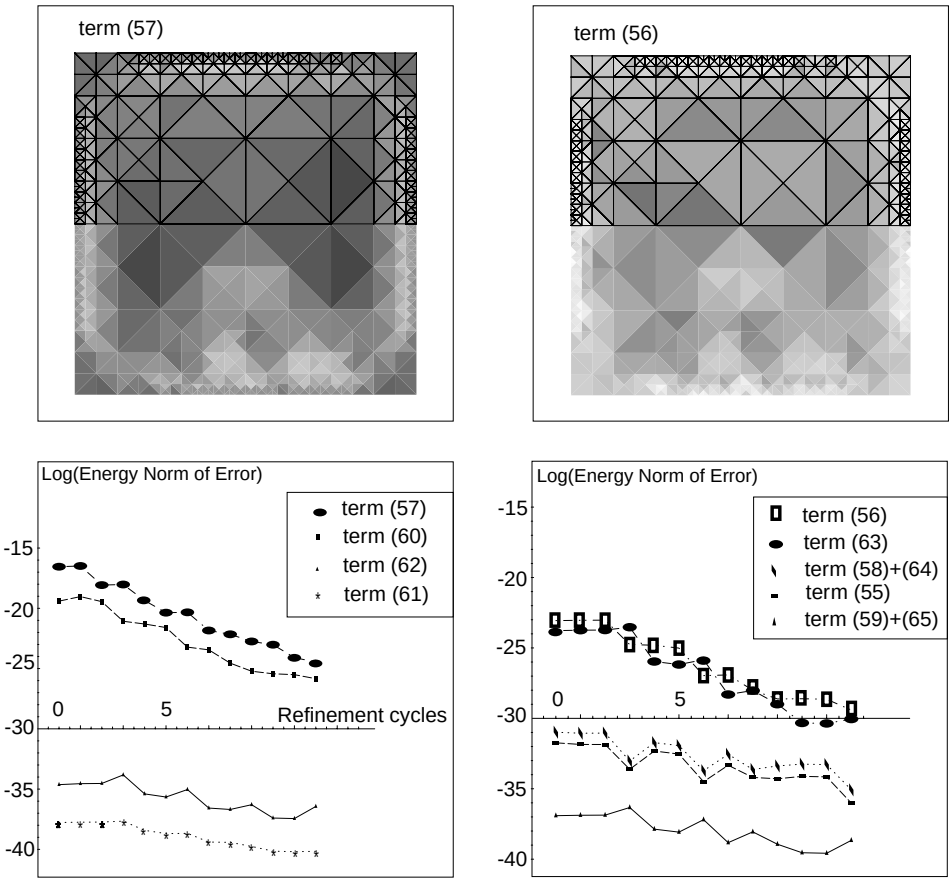

Fig. 12. Mechanical contributions to the total error of the thermo-mechanical problem. The lower left figure shows the reduction of the errors caused by inaccuracies of the computed membrane field. The dominant contributions are those involving the deviation of computed in-plane body force from the one that is prescribed (2D distribution shown above). The minor contributions are those which arise due to the coupling of the in-plane and the out-of-plane displacement field. They are only present where the structure is multi-layered. The figure on the lower right depicts the errors caused by the bending field. Here, the largest values (2D distribution shown above) are computed using the first order moments of the elasticity tensor and thus are related to the coupling of the fields. Both the membrane and bending errors are minor to the errors present in the temperature field.

as an actuator. The thin structure here consists of a ground layer and a piezoelectric layer and is actuated by a potential difference. The potential is applied on the bottom and the top of the structure as sketched in Fig. 3 and therefore evokes a mechanical displacement according to the direct piezoelectric effect. In Fig. 13 we have displayed the complete bending behavior computed on an adapted mesh as well as the y-component of the membrane field.

We have used a PZT-4 layer as the piezoelectrically active material. PZT-4 belongs to the 6 mm crystal class such as, for example, ZnO. The unreduced, 3D piezoelectric charge constants $\boldsymbol{d}$, given in units of C/N, see Appendix B, have the form

$$\boldsymbol{d} = \begin{pmatrix} 0 & 0 & 0 & 0 & d_{15} & 0 \\ 0 & 0 & 0 & d_{15} & 0 & 0 \\ d_{31} & d_{31} & d_{33} & 0 & 0 & 0 \end{pmatrix}, \tag{81}$$

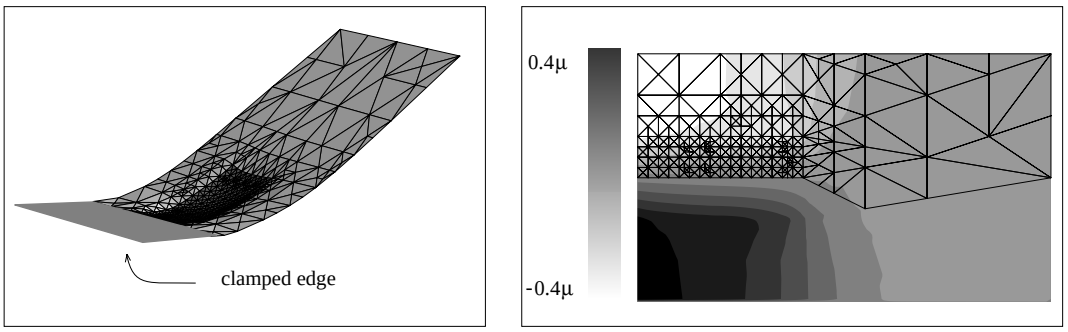

Fig. 13. Exaggerated deflection of the piezo-flap (left) and y-component of the horizontal displacement field (right). The structure has a clamped edge on its left boundary whereas the remaining part is mechanically free. The flap is driven by a voltage of 100 V in vertical direction. For clarity we have omitted a part of the underlying mesh.

where we have used the engineering notation for the last two indices of the third rank piezo-tensor. When also taking into account the numbers of non-zero and independent elastic coefficients for the crystal class under consideration, the tensor reduction yields a piezoelectric tensor that only has two independent components, which finally turn out to be identical since the relevant components of the reduced elastic tensor are also identical, $A_{11} = A_{22}$, and therefore,

$$\hat{\boldsymbol{\pi}} = \begin{pmatrix} 0 & 0 & 0 \\ 0 & 0 & 0 \\ d_{31}(A_{22} + A_{21}) & d_{31}(A_{21} + A_{22}) & 0 \end{pmatrix}. \tag{82}$$

Errors are biggest where the piezoelectric layer is located and at the layer stack interface. In this region, as can be seen in Fig. 15, the major mesh refinement occurs. Exemplarily we have displayed one mechanical contribution to the global error in Fig. 14. There, the elementwise distribution of inner element shear forces,

$$\|\nabla \cdot \boldsymbol{\sigma}_{w1}\|^2_{L^2(\mathrm{T})} h_{\mathrm{T}}^4, \tag{83}$$

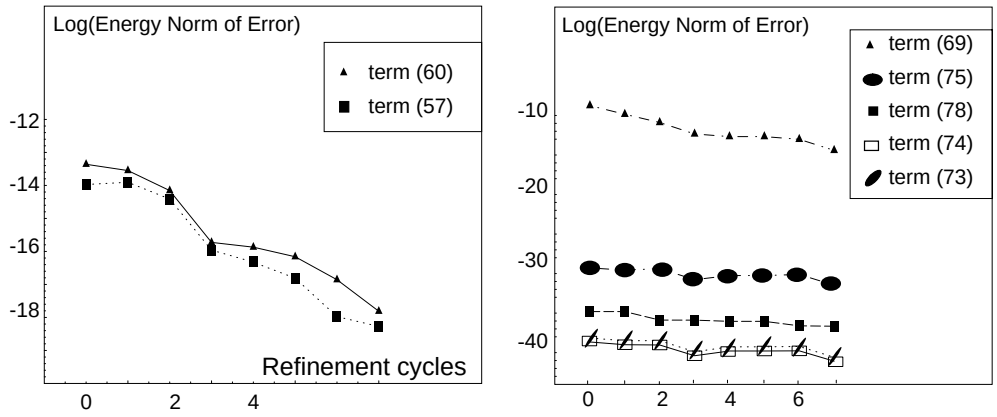

Fig. 14. The mechanical membrane contributions (left) and error contributions due to the direct and inverse piezoelectric effect and the pure electrostatic terms (right) to the overall error estimator. For the in-plane displacement field only two types of errors have significant values. The dominant error in this example are element residuals caused by the inverse piezoelectric effect.

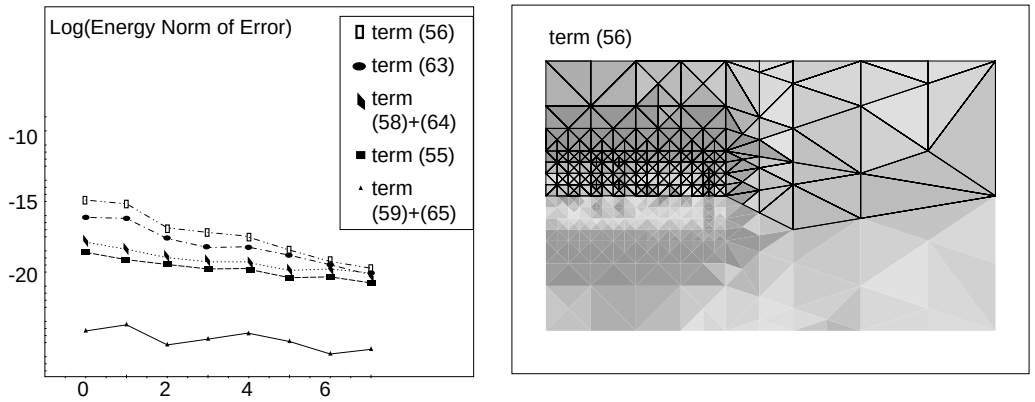

Fig. 15. The contributions of the bending field are highest for the element shear force residuals caused by the presence of a multi-layered structure and lowest for the jumps of the bending moments across element edges and the electrostatic contribution. The RHS shows the distribution of the largest pure mechanical error associated to the bending field in the seventh refinement cycle. These are inner element shear forces that physically are not allowed to exist. They are highest (dark) in the vicinity of the piezoelectrically active layer.

is displayed. These forces physically are not allowed to exist and are sought to be minimized during the refinement process. The contributions due to the residual stresses (69) caused by the inverse piezoelectric effect

$$\|\nabla_{2D} \cdot \boldsymbol{\sigma}_{P\phi}\|^2_{L^2(\mathrm{P})} h_{\mathrm{P}}^5 \tag{84}$$

are the principal contributions in this example. The other contributions that are related to the inverse piezoelectric effect are much smaller but may become considerably weightier when boundary conditions, material properties, structure thicknesses or loads are varied. The contributions of the direct piezoelectric effect are identically zero in the case we deal with the hexagonal crystal symmetry class 6 mm. The error contributions due to the direct piezoelectric effect are of the general shape, see (71), (72), (76) and (77),

$$\|\Xi_{3\mathrm{D}} \cdot \hat{\boldsymbol{\pi}} \cdot \upsilon\| = \|\Xi_{3\mathrm{D}} \cdot \hat{\boldsymbol{\pi}}_{i\alpha\beta} \upsilon_{\alpha\beta}\|, \tag{85}$$

where $\Xi_{3\mathrm{D}}$ either denotes the 3D divergence operator or the 3D face normal vector. Derivatives of the in-plane or the out-of-plane displacement fields are abbreviated by $\upsilon_{\alpha\beta}$ with the common two-index notation [20], greek indices ranging from one to two, latin indices ranging from one to three. Then, since the only non-vanishing components of $\hat{\boldsymbol{\pi}}$ are in its last row, (85) is zero for two possible reasons: either the prism's horizontal face normal's z-component vanishes or the electrical displacement $\hat{\boldsymbol{\pi}}_{i\alpha\beta}\upsilon_{\alpha\beta}$ does not depend on the z-coordinate and thus its partial derivative represented by the operator $\Xi_{3\mathrm{D}}$ vanishes identically.

9. Summary and conclusions

We have presented a method with which we can accurately simulate the structural behavior of thermo-mechanically and piezoelectrically driven multi-layer thin structures. Based on the Kirchhoff–Love plate theory a thin structure finite element model has been presented which not only covers the multi-physical nature of the structures but also takes into account horizontal and transversal anisotropy of the structures. For this thin structure model we applied residual error estimation techniques in order to get a local information about the error distribution in the energy norm. The single contributions to the total element error turn out to be of various nature. The contributions that are persistently present

when only considering the purely mechanical behavior are inner element residuals of forces and jumps of shear forces and bending moments. There are in addition those contributions which arise when the structure is multi-layered. The magnitude of each of these contributions varies according to the specified loads and material parameters. We have shown how these different contributions influence the way in which the mesh is refined. The reduction of the estimated energy error proves the reliability of the theoretically-derived error estimator.

A maximum refinement strategy is used for all meshes treated. A recursive algorithm is used to split the triangular elements in order to preserve shape regularity and to avoid hanging nodes. Several thin structures relevant in micro-devices serve as examples where the mesh adaptivity is demonstrated. Regions inside the structures, which are critical in the sense of structural singularities, are clearly identified by the method and accordingly refined such that the overall error is reduced to a minimum. By specifying the physical nature and the magnitude of the single error contributions a deeper insight into finite element simulation and the related errors is provided.

Future investigations will consider the implementation of other thin-structure models such as the Mindlin–Reissner model that in conjunction with a multi physical environment and together with improved finite element adaptivity may lead to enhanced simulation performance.

Acknowledgements

The authors express their sincere thanks to Stefano Taschini, who, through numerous discussions, and through making available his plate finite elements, helped along the progress of this work. This work was partially supported by the Deutsche Forschungsgemeinschaft (DFG) and the University of Freiburg.

Appendix A. Tensor operations

In this paper, we confine ourselves to the common notation for quantities that in the engineering language are denoted as tensors. The operations come in a handy size when using the notation of [52]:

Operation/Function space	Definition
Contraction	$(\boldsymbol{A}\cdot\boldsymbol{B})_{i\cdots jl\cdots m}=\sum_k A_{i\cdots jk}B_{kl\cdots m}$
Double contraction	$(\boldsymbol{A}:\boldsymbol{B})_{i\cdots jm\cdots n}=\sum_{kl} A_{i\cdots jkl}B_{klm\cdots n}$
Tensor product	$(\boldsymbol{AB})_{i\cdots jk\cdots l}=\sum_{kl} A_{i\cdots j}B_{k\cdots l}$
Transposition	$(\boldsymbol{A}^T)_{ij}=A_{ji}$
Symmetrization	$(\boldsymbol{A}^S)_{ij}=(A_{ij}+A_{ji})/2$
Gradient	$(\nabla\boldsymbol{A})_{ij\cdots k}=\partial A_{j\cdots k}=A_{j\cdots k,i}$
Divergence	$(\nabla\cdot\boldsymbol{A})_{j\cdots k}=\sum_i \partial A_{ij\cdots k}=\sum_i A_{ij\cdots k,i}$
$L^2(\Omega)$-inner product	$\int_\Omega \sum_{i\cdots j} A_{i\cdots j}B_{i\cdots j}\,\mathrm{d}\boldsymbol{x}$
Sobolev space of order m	$H^m(\Omega)=\{u : D^\alpha u\in L^2(\Omega)$ for all α such that $\lvert\alpha\rvert\leqslant m\}$

Appendix B. Tensor reduction for plates

For reasons of symmetry, the stress tensor has only six independent components [25] that can be arranged into two three-dimensional vectors

$$\boldsymbol{\sigma}_1 = \begin{pmatrix} \sigma_1 \\ \sigma_2 \\ \sigma_6 \end{pmatrix}, \quad \boldsymbol{\sigma}_2 = \begin{pmatrix} \sigma_3 \\ \sigma_4 \\ \sigma_5 \end{pmatrix}. \tag{B.1}$$

Also for the strain, its six independent components can be arranged into two 3D vectors

$$\boldsymbol{\epsilon}_1 = \begin{pmatrix} \epsilon_1 \\ \epsilon_2 \\ \epsilon_6 \end{pmatrix}, \quad \boldsymbol{\epsilon}_2 = \begin{pmatrix} \epsilon_3 \\ \epsilon_4 \\ \epsilon_5 \end{pmatrix}. \tag{B.2}$$

Consequently, the 21 independent components of the elastic tensor can be arranged into four 3D matrices

$$\begin{aligned} \boldsymbol{C}_{11} &= \begin{pmatrix} C_{11} & C_{12} & C_{16} \\ C_{21} & C_{22} & C_{26} \\ C_{61} & C_{62} & C_{66} \end{pmatrix}, \quad \boldsymbol{C}_{12} = \begin{pmatrix} C_{13} & C_{14} & C_{15} \\ C_{23} & C_{24} & C_{25} \\ C_{63} & C_{64} & C_{65} \end{pmatrix}, \\ \boldsymbol{C}_{21} &= \begin{pmatrix} C_{31} & C_{32} & C_{36} \\ C_{41} & C_{42} & C_{46} \\ C_{51} & C_{52} & C_{56} \end{pmatrix}, \quad \boldsymbol{C}_{12} = \begin{pmatrix} C_{33} & C_{34} & C_{35} \\ C_{43} & C_{44} & C_{45} \\ C_{53} & C_{54} & C_{55} \end{pmatrix}, \end{aligned} \tag{B.3}$$

relating the vectors $\boldsymbol{\sigma}_i$ with the vectors $\boldsymbol{\epsilon}_j$:

$$\begin{pmatrix} \boldsymbol{\sigma}_1 \\ \boldsymbol{\sigma}_2 \end{pmatrix} = \begin{pmatrix} \boldsymbol{C}_{11} & \boldsymbol{C}_{12} \\ \boldsymbol{C}_{21} & \boldsymbol{C}_{22} \end{pmatrix} \begin{pmatrix} \boldsymbol{\epsilon}_1 \\ \boldsymbol{\epsilon}_2 \end{pmatrix}. \tag{B.4}$$

When introducing the piezoelectric charge constants $\boldsymbol{d} = (\hat{d}_1\ \hat{d}_1)$ (unit $C/N = \mathrm{m/V}$) as

$$\boldsymbol{d}_1 = \begin{pmatrix} d_{11} & d_{12} & d_{16} \\ d_{21} & d_{22} & d_{26} \\ d_{61} & d_{62} & d_{66} \end{pmatrix}, \quad \boldsymbol{d}_2 = \begin{pmatrix} d_{13} & d_{14} & d_{15} \\ d_{23} & d_{24} & d_{25} \\ d_{63} & d_{64} & d_{65} \end{pmatrix}, \tag{B.5}$$

the stress then is given in terms of

$$\begin{pmatrix} \boldsymbol{\sigma}_1 \\ \boldsymbol{\sigma}_2 \end{pmatrix} = \begin{pmatrix} \boldsymbol{C}_{11} & \boldsymbol{C}_{12} \\ \boldsymbol{C}_{21} & \boldsymbol{C}_{22} \end{pmatrix} \left[\begin{pmatrix} \boldsymbol{\epsilon}_1 \\ \boldsymbol{\epsilon}_2 \end{pmatrix} - \begin{pmatrix} \hat{d}_1^T \\ \hat{d}_2^T \end{pmatrix} \boldsymbol{E} \right]. \tag{B.6}$$

The relation for the plane stress when applying the Kirchhoff–Love condition [15] then reads

$$\boldsymbol{\sigma}_1 = (\boldsymbol{\epsilon}_1 - \hat{d}_1 \boldsymbol{E}) \equiv \hat{\boldsymbol{A}} : \boldsymbol{\epsilon} - \hat{\boldsymbol{\pi}}^T \cdot \boldsymbol{E} \tag{B.7}$$

having defined the reduced piezo tensor as

$$\hat{\boldsymbol{\pi}}^T = \hat{\boldsymbol{A}} \cdot \hat{d}_1^T, \tag{B.8}$$

$\hat{\boldsymbol{A}}$ being the reduced elasticity tensor,

$$\hat{\boldsymbol{A}} = \boldsymbol{C}_{11} - \boldsymbol{C}_{12} \boldsymbol{C}_{22}^{-1} \boldsymbol{C}_{21}. \tag{B.9}$$

The equation for the electrical displacement uses reduced quantities, too:

$$\boldsymbol{D} = (\hat{\boldsymbol{d}}_1\ \hat{\boldsymbol{d}}_1) \begin{pmatrix} \boldsymbol{C}_{11} & \boldsymbol{C}_{12} \\ \boldsymbol{C}_{21} & \boldsymbol{C}_{22} \end{pmatrix} \begin{pmatrix} \boldsymbol{\epsilon}_1 \\ \boldsymbol{\epsilon}_2 \end{pmatrix} + \boldsymbol{\chi} \boldsymbol{E}, \tag{B.10}$$

where the piezoelectric charge constants are related to the piezoelectric stress coefficients $\boldsymbol{\pi}$ by

$$\boldsymbol{\pi} = \boldsymbol{d} : \boldsymbol{C}. \tag{B.11}$$

Introducing the relation for the strain $\boldsymbol{\epsilon}_2$ obtained from (B.6) by the requirement that $\boldsymbol{\sigma}_2$ vanishes, turns (B.10) into

$$\boldsymbol{D} = (\hat{\boldsymbol{d}}_1\ \hat{\boldsymbol{d}}_1)\begin{pmatrix} \boldsymbol{C}_{11} & \boldsymbol{C}_{12} \\ \boldsymbol{C}_{21} & \boldsymbol{C}_{22} \end{pmatrix}\begin{pmatrix} \boldsymbol{\epsilon}_1 \\ (\boldsymbol{C}_{22}^{-1}\boldsymbol{C}_{21}\hat{\boldsymbol{d}}_1^T + \hat{\boldsymbol{d}}_2^T)\boldsymbol{E} - \boldsymbol{C}_{22}^{-1}\boldsymbol{C}_{21}\boldsymbol{\epsilon}_1 \end{pmatrix} + \boldsymbol{\chi}\boldsymbol{E} \tag{B.12}$$

such that the dependence is only on $\boldsymbol{\epsilon}_1$. Further calculation yields

$$\boldsymbol{D} = \hat{\boldsymbol{d}}_1\hat{\boldsymbol{A}}\boldsymbol{\epsilon}_1 - \hat{\boldsymbol{d}}_1\boldsymbol{C}_{12}\hat{\boldsymbol{d}}_2^T\boldsymbol{E} - \hat{\boldsymbol{d}}_1(\boldsymbol{C}_{11} - \hat{\boldsymbol{A}})\hat{\boldsymbol{d}}_1^T\boldsymbol{E} + (\hat{d}_2\boldsymbol{C}_{22}\hat{\boldsymbol{d}}_2^T + \hat{\boldsymbol{d}}_2\boldsymbol{C}_{21}\hat{\boldsymbol{d}}_1^T)\boldsymbol{E} + \boldsymbol{\chi}\boldsymbol{E} \tag{B.13}$$

which, when defining

$$\hat{\boldsymbol{\chi}} \equiv (\hat{\boldsymbol{d}}_2\boldsymbol{C}_{22}\hat{\boldsymbol{d}}_2^T + \hat{\boldsymbol{d}}_2\boldsymbol{C}_{21}\hat{\boldsymbol{d}}_1^T) - (\hat{\boldsymbol{d}}_1\boldsymbol{C}_{12}\hat{\boldsymbol{d}}_2^T + \hat{\boldsymbol{d}}_1(\boldsymbol{C}_{11} - \hat{\boldsymbol{A}})\hat{\boldsymbol{d}}_1^T) + \boldsymbol{\chi} \tag{B.14}$$

can be recast into

$$\boldsymbol{D} = \hat{\boldsymbol{\pi}} \cdot \boldsymbol{\epsilon} + \hat{\boldsymbol{\chi}} \cdot \boldsymbol{E}. \tag{B.15}$$

A similar relation holds for thermally induced stresses.

References

[1] H. Baltes, R. Castagnetti, Magnetic sensors, in: S.M. Sze (Ed.), Semiconductor Sensors, Wiley/Interscience, New York, 1994, pp. 205–270 (Chapter 5).

[2] S. Taschini, J. Müller, A. Greiner, M. Emmenegger, H. Baltes, J.G. Korvink, Accurate modeling and simulation of thermo-mechanical microsystem dynamics, Comput. Modeling Eng. Sci. 1 (2000) 31–44.

[3] I. Babuška, W. Reinboldt, Error estimates for adaptive finite element computations, SIAM J. Numer. Anal. 15 (1978) 736–754.

[4] I. Babuška, O.C. Zienkiewicz, J.P. Gago, E.R.de A. Oliveira (Eds.), Accuracy Estimates and Adaptive Refinements in Finite Element Computations, Wiley, New York, 1986.

[5] R.E. Bank, A. Weiser, Some a posteriori error estimators for elliptic partial differential equations, Math. Comput. 44 (1985) 283–301.

[6] O.C. Zienkiewicz, J.Z. Zhu, A simple error estimator and adaptive procedure for practical engineering analysis, Int. J. Numer. Methods Eng. 24 (1987) 337–357.

[7] R. Verfürth, A Review of A Posteriori Error Estimation and Adaptive Mesh Refinement Techniques, Wiley–Teubner, Chichester–New York–Stuttgart, 1996.

[8] K. Eriksson, C. Johnson, Adaptive finite element methods for parabolic problems II, SIAM J. Numer. Anal. 32 (3) (1995) 706–740.

[9] M. Ainsworth, J.T. Oden, A Posteriori Error Estimation in Finite Element Analysis, Wiley, New York, 2000.

[10] J.T. Oden, K.S. Vemaganti, Estimation of Local Modeling Error and Goal-Oriented Adaptive Modeling of Heterogeneous Materials I. Error Estimates and Adaptive Algorithms, J. Comput. Phys. (2000), doi: 10.1006/jcph.2000.6585.

[11] N. Provatas, N. Goldenfeld, J. Dantzig, Adaptive Mesh Refinement Computation of Solidification Microstructures Using Dynamic Data Structures, J. Comput. Phys. (1999), doi: 10.1006/jcph.1998.612.

[12] O.C. Zienkiewicz, J.Z. Zhu, Error estimates and adaptive refinement for plate bending problems, Int. J. Numer. Methods Eng. 28 (1989) 2839–2853.

[13] C.K. Lee, R.E. Hobbs, Automatic Adaptive Refinemement for Plate Bending Problems Using Reissner–Mindlin Plate Bending Elements, Int. J. Numer. Methods Eng. 41 (1998) 1–63.

[14] P.G. Ciarlet, Mathematical Elasticity, Theory of Plates, vol. II, North Holland, Amsterdam, 1997.

[15] P.G. Ciarlet, Plates and junctions in elastic multi-structures, Masson Springer, Paris, 1990.

[16] F. Brezzi, M. Fortin, Numerical approximation of Mindlin–Reissner-plates, Math. Comput. 47 (1986) 151–158.

[17] D.N. Arnold, R.S. Falk, A uniformly accurate finite element method for the Reissner–Mindlin plate, SIAM J. Numer. Anal. 26 (6) (1989) 1276–1290.

[18] E. Hinton, H.C. Huang, A family of quadrilateral Mindlin plate elements with substitute shear strain fields, Comput. Struct. 23 (1986) 409–431.
[19] H.C. Huang, E. Hinton, A nine node Lagrangian Mindlin plate element with enhanced shear interpolation, Eng. Comput. 1 (1984) 369–379.
[20] H.C. Huang, Static and Dynamic Analyses of Plates and Shells. Theory, Software and Applications, Springer, Berlin, 1989.
[21] K.Y. Sze, An explicit hybrid-stabilized 9-node Lagrangian shell element, Comput. Methods Appl. Mech. Eng. 117 (1994) 361–379.
[22] F.G. Flores, E. Onate, F. Zarate, New assumed strain triangles for non linear shell analysis, Comput. Mech. 17 (1995) 107–114.
[23] J. Müller, J.G. Korvink, Automatic accuracy control for large aspect ratio multi-layer MEMS simulation, in: Proc. Eurosensors XIV, Kopenhagen, 1999, pp. 277–278.
[24] M.C. Rivara, Algorithms for refining triangular grids suitable for adaptive and multigrid techniques, Int. J. Numer. Methods Eng. 20 (1984) 745–756.
[25] J.F. Nye, Physical Properties of Crystals, Oxford University Press, Oxford, 1985.
[26] G. Kirchhoff, Über das Gleichgewicht und die Bewegung einer elastischen Scheibe, J. Reine Angew. Math. 40 (1850) 51–58.
[27] G. Kirchhoff, Vorlesungen über Mathematische Physik, Mechanik, Leipzig, 1876.
[28] A.E.H Love, The Mathematical Theory of Elasticity, Cambridge University Press, Cambridge, MA, 1934.
[29] J.H. Argyris, I. Fried, D.W. Scharpf, The TUBA family of plate elements for the matrix displacement method, Aero. J. Royal Aeronaut. Soc. 72 (1968) 701–709.
[30] M. Bernadou, Finite Element Methods for Thin Shell Problems, Wiley, Chichester, UK, 1996.
[31] I. Babuška, L. Li, The problem of plate modeling: theoretical and computational result, Comput. Methods Appl. Mech. Eng. 100 (1992) 249–273.
[32] N.V.R. Rao, M. Ozakca, E. Hinton, A study of boundary layers in plates using Mindlin–Reissner and 3D elements, Int. J. Numer. Methods Eng. 33 (1992) 1305–1320.
[33] E. Hinton, H.C. Huang, Shear forces and twisting moments in plates using Mindlin elements, Eng. Comput. 3 (1986) 129–142.
[34] A. Schmidt, Computation of Three Dimensional Dendrites with Finite Elements, J. Comput. Phys. (1996), doi: 10.1006/jcph.1996.0095.
[35] Ph. Clément, Approximation by finite element functions using local regularization, RAIRO Anal. Numer. 2 (1975) 77–84.
[36] E. Bänsch, Local mesh refinement in 2 and 3 dimensions, Impact Comput. Sci. Eng. 3 (1991) 181–191.
[37] I.G. Rosenberg, F. Stenger, A lower bound on the angle of triangles constructed by bisecting the longest side, Math. Comput. 29 (1975) 390–395.
[38] S.W. Sloan, A fast algorithm for generating constrained Delaunay triangulations, Comput. Struct. 47 (1993) 441–450.
[39] P.L. George, E. Seveno, The advancing-front mesh generation method revisited, Int. J. Numer. Methods Eng. 37 (1994) 3605–3619.
[40] E.B. Christoffel, Sul problema delle temperature stazonarie e la rappresentazione di una data super cie, Ann. Math. Pura Appl. Serie II 1 (1868) 89–103.
[41] The MathWorks: Developers of MATLAB and Simulink for Technical Computing. Available from: <http://www.mathworks.com/>.
[42] T. Strouboulis, K.A. Haque, Recent experiences with error estimation and adaptivity. I. Review of error estimators for scalar elliptic problems, Comput. Methods Appl. Mech. Eng. 97 (1992) 399–436.
[43] T. Strouboulis, K.A. Haque, Recent experiences with error estimation and adaptivity. II. Error estimation for *h*-adaptive approximations on grids of triangles and quadrilaterals, Comput. Methods Appl. Mech. Eng. 100 (1992) 359–430.
[44] J.N. Reddy, An Introduction to the Finite Element Method, McGraw-Hill, New York, 1993.
[45] J. Müller, Accurate FE-simulation of three-dimensional microstructures, Ph.D. Dissertation, University of Freiburg, Germany, 2001.
[46] J. Mueller, J.G. Korvink, Automatic mesh adaptivity for finite element simulation of multi-layer MEMS, Materials and device characterisation in micromachining III, in: Proc. SPIE 4175, Santa Clara, 2000, pp. 82–93.
[47] C. Hagleitner, A. Hierlemann, D. Lange, A. Kummer, N. Kerness, O. Brand, H. Baltes, Smart single-chip gas sensor microsystem, Nature 414 (2001) 293–296.
[48] D. Lange, T. Akiyama, C. Hagleitner, A. Tonin, H.R. Hidber, P. Niedermann, U. Staufer, N.F. de Rooij, O. Brand, H. Baltes, Parallel scanning AFM with on-chip circuitry in CMOS technology, in: Proc. IEEE MEMS '99, Orlando, 1999, pp. 447–453.
[49] G. Strang, G. Fix, An Analysis of the Finite Element Method, Wellesley-Cambridge, Wellesley, 1997.
[50] O. Brand, H. Baltes, Micromachined resonant sensors: an overview, in: H. Baltes, W. Göpel, J. Hesse (Eds.), Sensors Update, vol. 4, Wiley–VCH Verlag, Weinheim, New York, 1998, pp. 3–51.
[51] S. Koller, O. Brand, P.M. Sarro, M.J. Vellekoop, H. Baltes, Piezoelectric ZnO membrane resonators for liquid property sensing, in: Proc. of Eurosensors XIII, The Hague, The Netherlands, 1999, pp. 677–680.
[52] J.W. Gibbs, E.B. Wilson, Vector Analysis, Yale University Press, New Haven, 1901.